Spring 5-2014

Calculation and Experimental Verification of Longitudinal Spatial Hole Burning in High-Power Semiconductor Lasers

Ting Hao
haot@rose-hulman.edu

Calculation and Experimental Verification of Longitudinal Spatial Hole Burning in High-Power Semiconductor Lasers

A Thesis

Submitted to the Faculty

of

Rose-Hulman Institute of Technology

by

Ting Hao

In Partial Fulfillment of the Requirements for the Degree

of

Master of Science in Optical Engineering

May 2014

ROSE-HULMAN INSTITUTE OF TECHNOLOGY

Final Examination Report

Ting Hao — Optical Engineering

Name — Graduate Major

Thesis Title: Calculation and Experimental Verification of Longitudinal Spatial Hole Burning in High-Power Semiconductor Lasers

DATE OF EXAM: May 1, 2014

EXAMINATION COMMITTEE:

	Thesis Advisory Committee	Department
Thesis Advisor:	Paul Leisher	PHOE
	Kurt Bryan	MA
	Michael McInerney	PHOE

PASSED X **FAILED** _____

ABSTRACT

Ting Hao

M.S.O.E

Rose-Hulman Institute of Technology

May 2014

Calculation and Experimental Verification of Longitudinal Spatial Hole Burning in High-Power Semiconductor Lasers

Thesis Advisor: Dr. Paul Leisher

Longitudinal spatial hole burning (LSHB) is believed to be one of the limiting factors in scaling the output power of high-power semiconductor lasers. In this work, a self-consistent simulation of LSHB was performed to investigate the non-uniform longitudinal photon density distribution, carrier density distribution, and gain distribution in a high-power semiconductor laser. The calculation is based on a modification to the semiconductor laser rate equations and solved using a finite difference approach, with Newton's method employed to numerically solve the differential equations. The impact of LSHB on output power was analyzed with different parameters, including injection current, cavity length, and wavelength. Experimental verification was carried out by direct observation of spontaneous emission from a window patterned into the top contact of an 808 nm high-power semiconductor laser. The experimental results are in agreement with calculated results.

ACKNOWLEDGEMENTS

I would like to express the deepest appreciation to my advisor, Dr. Paul Leisher, for his patient guidance and great help throughout this project. I would like to thank my committee members: Dr. Michael McInerney and Dr. Kurt Bryan, for their helpful suggestions in this project. I also would like to thank my classmate, Junyeob Song, for his assistance in the experimental work. In addition, I would like to thank my family for their great moral support.

TABLE OF CONTENTS

LIST OF FIGURES

LIST OF TABLES

1. INTRODUCTION

1.1 Semiconductor Lasers Overview

Since it was discovered in 1962, the semiconductor laser has brought great revolution in science and industry [1]. Semiconductor lasers are distinguished from other types of lasers primarily by their ability to be pumped directly by electrical current. This results in a much more efficient operation than other types of lasers. The overall power conversion efficiency can reach >70% [2]. Therefore, semiconductor lasers have a distinct advantage in high-power applications where heat generation and removal are the limiting factors. Also, size is another striking difference between semiconductor lasers and others. With the technology of metal organic chemical vapor deposition (MOCVD), quantum-well semiconductor lasers can be fabricated with active layer thickness on the order of 10 nm [1]. The whole package of a common semiconductor laser including mounting and wire bonding is on the order of cubic centimeter, which makes it a competitive candidate for integrated applications. Figure 1.1 shows several kinds of common semiconductor lasers [3] [4].

Figure 1.1: Several kinds of common semiconductor lasers [3] [4]

Another advantage of semiconductor lasers, which has led to their widespread use, is their high reliability and long lifetime. The useful lifetime of semiconductor lasers are often measured in tens to hundreds of years, while the lifetime of gas or solid-state lasers are measured in thousands of hours [5].

Among all types of semiconductor lasers, high-power semiconductor lasers refer to those having output powers above one watt. These devices can be used in applications such as fiber optic communications, materials processing technologies, medical therapy, military defense, free-space communications, and many others. Practical lasers must emit light in a narrow beam, which implies a lateral confinement is necessary. Most low-power semiconductor lasers used in data storage and telecommunications are index-guided, as a high-quality and single-mode laser beam is required in these applications. However, high-power semiconductor lasers, whose applications often do not require the single-mode output, are usually gain-guided [6]. Gain-guided technology confines charge carriers by designing the gain region only at the center of active layer, and it can achieve high output power through simple fabrication process. Figure 1.2 shows the structure of a typical gain-guided high-power edge emitting semiconductor laser.

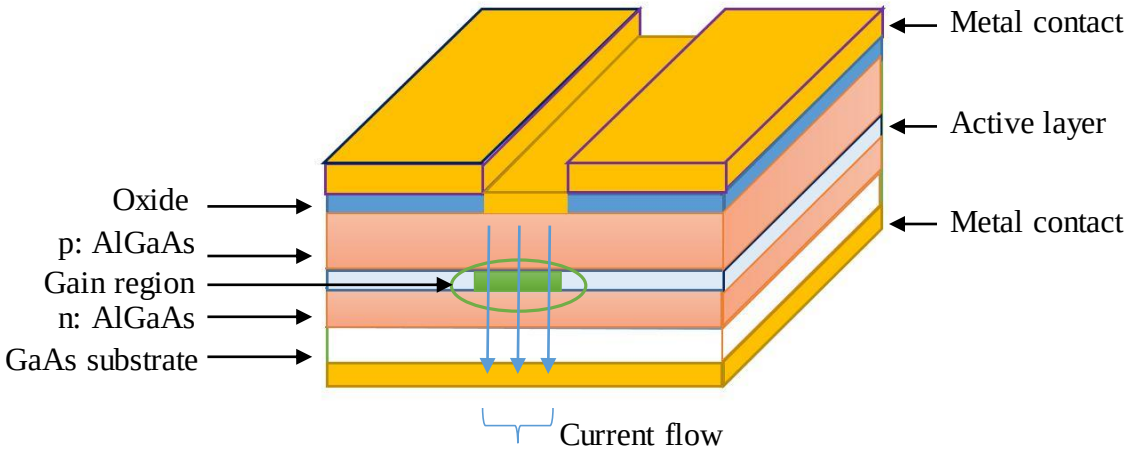

Figure 1.2: The structure of a gain-guided edge emitting semiconductor laser

Like other types of lasers, semiconductor lasers include three main components: input pump power, gain, and a resonant cavity. Figure 1.3 shows a schematic longitudinal diagram of a semiconductor laser [7].

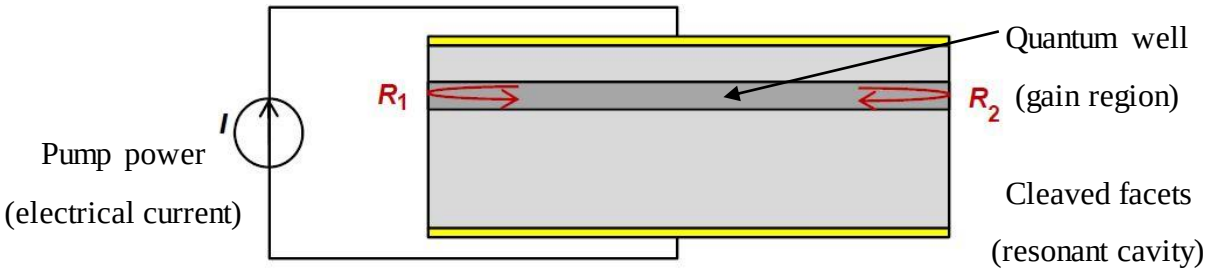

Figure 1.3: Schematic longitudinal diagram of a semiconductor laser [7]

The input power for semiconductor lasers can be electrical or optical energy, though most semiconductor lasers are pumped with electrical current. The gain media in semiconductor lasers is a semiconductor material such as AlGaAs, InP and so on. Optical gain is achieved by electron-hole recombination which generates photons through stimulated emission. There are three main interband transition processes in the active region: absorption, spontaneous emission, and stimulated emission. For optical gain to occur, the probability of stimulated emission must be greater than probability of absorption. This occurs when the quasi-Fermi energy separate $F_n - F_p$ exceeds the band-gap energy E_g and is referred to as population inversion. If the roundtrip gain is sufficient to overcome the roundtrip loss for a resonant optical mode, this mode is said to have reached threshold, and lasing action begins. The resonant cavity, which is commonly made by cleaving facets, provides the necessary feedback for the emission to be amplified, so that lasing oscillation can be sustained above threshold. Figure 1.4 shows the measured light-current-voltage (LIV) curve for a typical 808 nm high-power semiconductor laser.

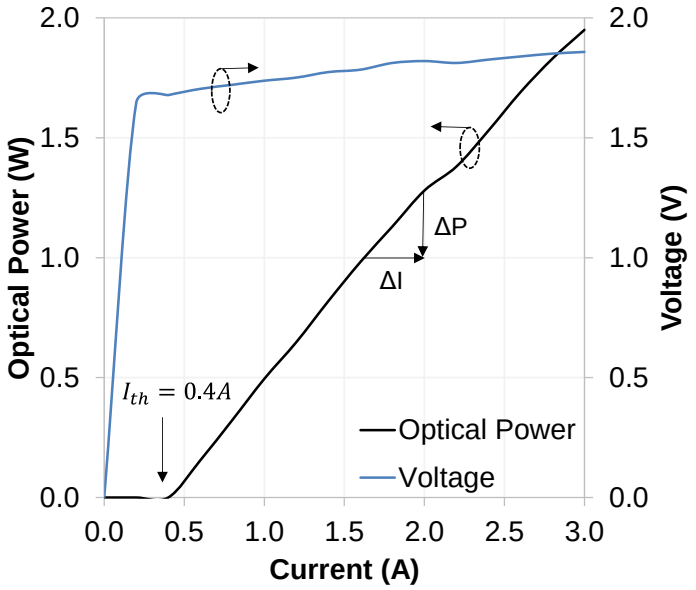

Figure 1.4: LIV characteristic of a typical semiconductor laser

I_{th} represents the threshold current at which the semiconductor laser begins to lase. Beyond threshold, the output power increases almost linearly with injection current, shown in Equation 1.1 and Figure 1.4. Here $\frac{h\nu}{q}$ is the photon voltage. Slope efficiency is defined as the ratio of laser output power to current injected (ΔP/ΔI), and has units W/A. Differential quantum efficiency (DQE) η_d represents the number of photons emitted from the laser per electron-hole pair injected and equals to the slope efficiency divided by the photon voltage. Equation 1.2 shows the relation of voltage and current [8]. Since the semiconductor laser is based on the p-n junction, and it doesn't turn on exactly at $\frac{h\nu}{q}$, ΔV_{diode} is added here to make $V_{turn-on} = \frac{h\nu}{q} + \Delta V_{diode}$. Also, due to the existence of series resistance R_s, the applied voltage is not constant with current.

$$P_{out} \cong \eta_d \frac{h\nu}{q}(I - I_{th}) \tag{1.1}$$

$$V_{applied} \cong \frac{h\nu}{q} + \Delta V_{diode} + R_s I \tag{1.2}$$

To improve slope efficiency, the laser structure design must be carefully engineered. The separate confinement heterostructure (SCH) is one design approach which is widely used nowadays, as it provides confinement of both carriers and photons in a thin active region. Figure 1.5 shows the facet-view diagram of a SCH semiconductor laser [9]. Figure 1.6 shows the corresponding energy band diagram.

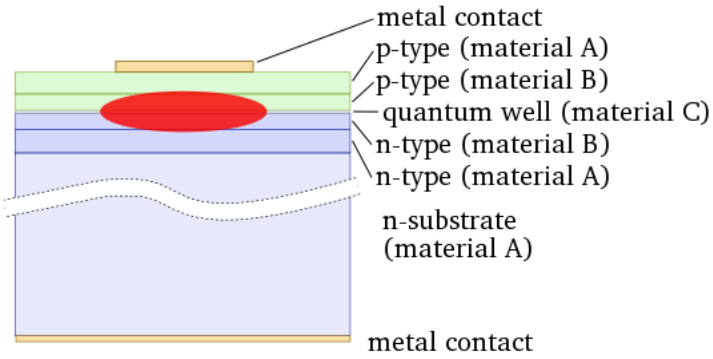

Figure 1.5: Facet-view diagram of a SCH semiconductor laser [9]

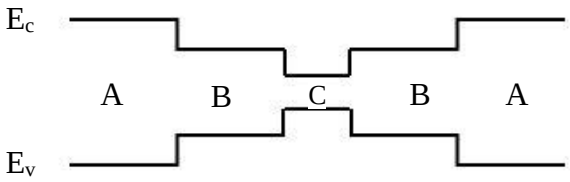

Figure 1.6: Band diagram of a SCH semiconductor laser

The thin quantum-well region is used to confine carriers, because the density of states function of carriers in the quantum well system has an abrupt edge that concentrates carriers in energy states that contribute to laser action [10]. Outside the quantum-well, the layers of low band-gap material are sandwiched between two high band-gap layers so that light generated in the active region is guided in this region and to ensure the optical mode does not overlap the heavily doped cladding material (where optical absorption loss is high).

1.2 Rate Equations

The physical operation of semiconductor lasers can be described by a set of coupled rate equations, which describe the relation of photon density, carrier density, and optical gain. Let N be carrier density and N_p be photon density, the standard rate equations [11] are shown in Equations 1.3 and 1.4.

$$\frac{dN}{dt} = \frac{\eta_i I}{qV} - \frac{N}{\tau} - R_{st} \tag{1.3}$$

$$\frac{dN_p}{dt} = \Gamma R_{st} + \Gamma \beta_{sp} R_{sp} - \frac{N_p}{\tau_p} \tag{1.4}$$

Equation 1.3 describes the rate of change of carrier density. The first term on the right side stands for injection rate of carriers; the second term stands for the recombination rate consuming carriers but not resulting laser output; the last term stands for the stimulated emission rate, which electrons and holes recombine to generate photons. Here, η_i is defined as intrinsic efficiency, which is the ratio of electrons making radiative transition to total electrons. I is defined as injection current, q as electron charge, and V as active region volume. τ is carrier lifetime which mainly includes Shockley-Read-Hall recombination, spontaneous radiative recombination, and Auger recombination [12]. Figure 1.7 shows the schematic band-gap diagram of these processes, and each is discussed further.

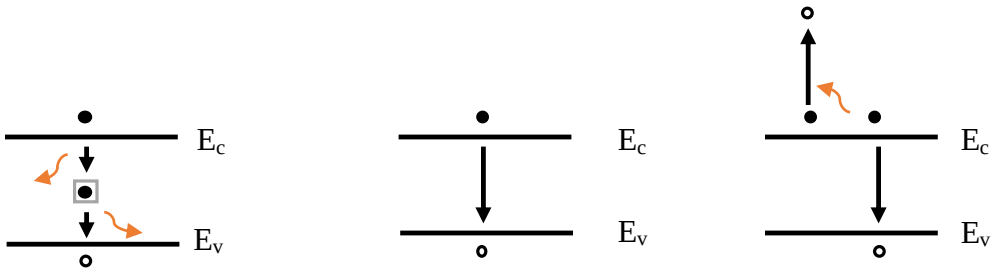

Figure 1.7: Schematic band-gap diagram of SRH, spontaneous, and Auger recombination

Shockley-Read-Hall recombination is mainly caused by defects in the lattice or impurities. An energy level between the conduction band and valence band traps electrons temporarily before releasing it to the valence band. The energy is dissipated by heat instead of light. Spontaneous radiative recombination refers to the optical generation which occurs spontaneously. Spontaneous emission is a random process, occurring in all directions, and does not contribute to laser output. Auger recombination is a three-carrier process in which an electron and a hole recombine, transferring their energy to another electron which moves up to a higher energy state [13]. Auger recombination and SRH are non-radiative processes which release excess energy as heat. These three processes can be used to approximate an effective carrier lifetime (in the absence of stimulated emission), as shown in Equation 1.5, with coefficients A, B, and C, respectively.

$$\frac{1}{\tau} = AN + BN^2 + CN^3 \tag{1.5}$$

Electron hole pairs can also recombine due to stimulated emission. This rate is directly related to photon density, as shown in Equation 1.6. Here, v_g is photon group velocity in semiconductor material, and g is the material gain. The gain is also a function of carrier density, and this dependence can be approximated by a log function, shown in Equation 1.7. N_{tr} is transparency carrier density, at which the probability of stimulated emission equals the probability of absorption (no gain, no loss).

$$R_{st} = v_g g N_p \tag{1.6}$$

$$g \approx g_0 \ln\left(\frac{N}{N_{tr}}\right) \tag{1.7}$$

Equation 1.4 describes the rate of change of photon density. The first term stands for photon density accumulating in the whole cavity by stimulated emission. Γ is modal overlap parameter, which is equal to the ratio of mode energy in the active region to the total energy. The second term

stands for photons contributed by spontaneous emission, and β_{sp} is fraction of spontaneous emission which couples into the lasing mode (for large cavity lasers such as in high-power BAL's, $\beta_{sp} \approx 0$). The last term represents for photon loss rate, and τ_p is the photon lifetime, which is the average time a photon stays in the cavity before it is absorbed or emitted.

The rate equations can be used to explain the operation of semiconductor lasers. Figure 1.8 shows the relation of carrier density, gain, and photon density, with increasing current.

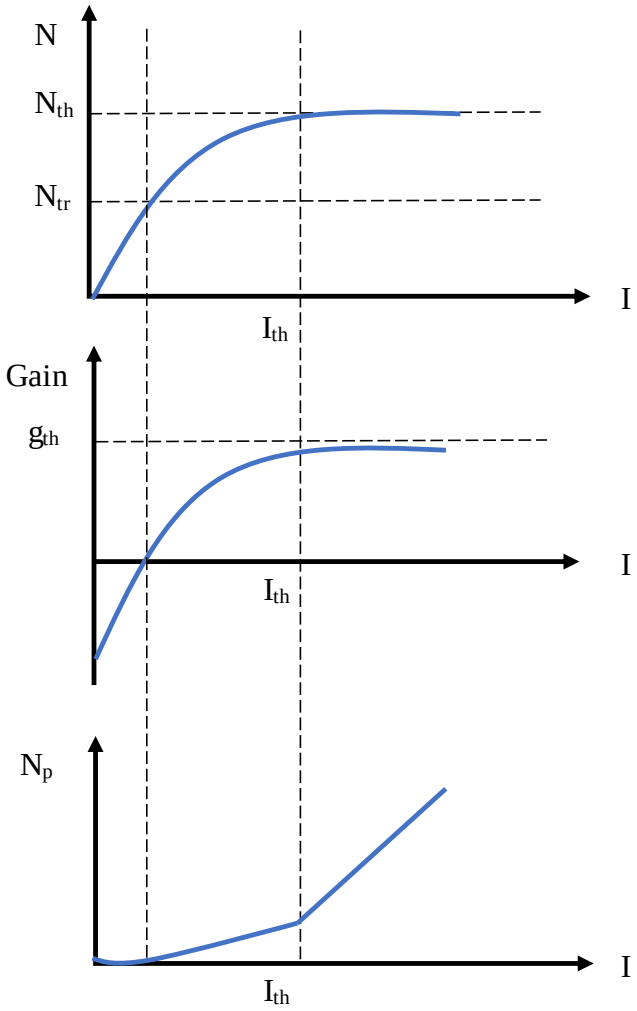

Figure 1.8: The profiles of carrier, gain, and photon with increasing current

When injection current is below threshold and the carrier density is below transparency, optical absorption is probabilistically favored over stimulated emission, leading to a negative gain and almost no photon generation. As current increases, the carrier density (Equation 1.3) will increase. The gain will become positive when carrier density exceed transparency carrier density. However, below threshold, R_{st} is not large enough to offset the photon loss rate from the cavity. According to Equation 1.4, the photon density in the cavity is therefore still very small and is mainly dominated by spontaneous emission. As current increases further, the carrier density reaches threshold N_{th}, corresponding to a gain of g_{th}. From this point, photon generation balances photon loss, and laser action begins. When the current is above threshold, the photon density becomes so large that R_{st}, which is directly related to photon density, becomes large enough to prevent the carrier density from further increasing, as shown in Equation 1.3. This results in the carrier density saturating at N_{th}. This condition is called gain pinning (or gain clamping) and is the key to why semiconductor lasers can be so efficient. Essentially, every additional electron-hole pair which is injected into the quantum well results in the immediate emission of a photon from the cavity.

In this thesis, steady state operation is concerned, so the left sides of Equation 1.3 and 1.4 are set to zero. Since the photon density generated by spontaneous emission is quite small compared with stimulated emission, $\Gamma\beta_{sp}R_{sp}$ in Equation 1.4 is ignored. At this point, no longitudinal spatial hole burning is considered, and the carrier density and gain are assumed to be saturated at their constant threshold values during lasing operation. Therefore, the time dependent differential equations evolve into an ordinary equation set, shown by Equation 1.8, 1.9, and 1.10, which can be solved algebraically. An example calculation for a 980 nm high-power

semiconductor laser was carried out, and the main procedures are presented below. Detailed calculation and results are shown in Appendix A.

$$0 = \frac{\eta_i I}{qV} - \frac{N_{th}}{\tau} - v_g g_{th} N_p \tag{1.8}$$

$$0 = \Gamma v_g g_{th} N_p - \frac{N_p}{\tau_p} \tag{1.9}$$

$$g_{th} \approx g_0 \ln\left(\frac{N_{th}}{N_{tr}}\right) \tag{1.10}$$

By substituting Equation 1.10 into Equation 1.9, one can obtain the solution of threshold carrier density N_{th}. Then the threshold gain g_{th} can be solved by Equation 1.10. By Substituting N_{th} and g_{th} into Equation 1.8, the function of photon density with injection current can be obtained. Threshold current can also be solved based on threshold carrier density [5] shown in Equation 1.11.

$$I_{th} = \frac{N_{th} q V}{\tau_e \eta_i} \tag{1.11}$$

Here, q is electron charge, V is the volume of laser cavity, τ_e is the carrier life time, and η_i is internal quantum efficiency. The output power is determined by the product of photon density, photon energy, effective volume of optical mode, and photon escape rate [12], which can be calculated by Equation 1.12.

$$P_{output} = N_p \frac{hc}{\lambda} \frac{V}{\Gamma} v_g a_m \tag{1.12}$$

Here, a_m is the mirror loss, and is shown in Equation 1.13

$$a_m = \frac{1}{2L} \ln\left(\frac{1}{R_1 R_2}\right) \tag{1.13}$$

The lasing threshold condition, in which optical gain equals the total loss, including mirror loss and internal loss, is shown in Equation 1.14.

$$\Gamma g_{th} = a_m + a_i = \frac{1}{2L}\ln\left(\frac{1}{R_1 R_2}\right) + a_i \tag{1.14}$$

Figure 1.9 shows the calculated power versus current (P-I) characteristic of the example 980 nm semiconductor laser. For this device, the slope efficiency is 1W/A, and threshold current is 0.85A. Note that the effect of self-heating is neglected in this simple model, and hence the dependence of power on current is precisely linear.

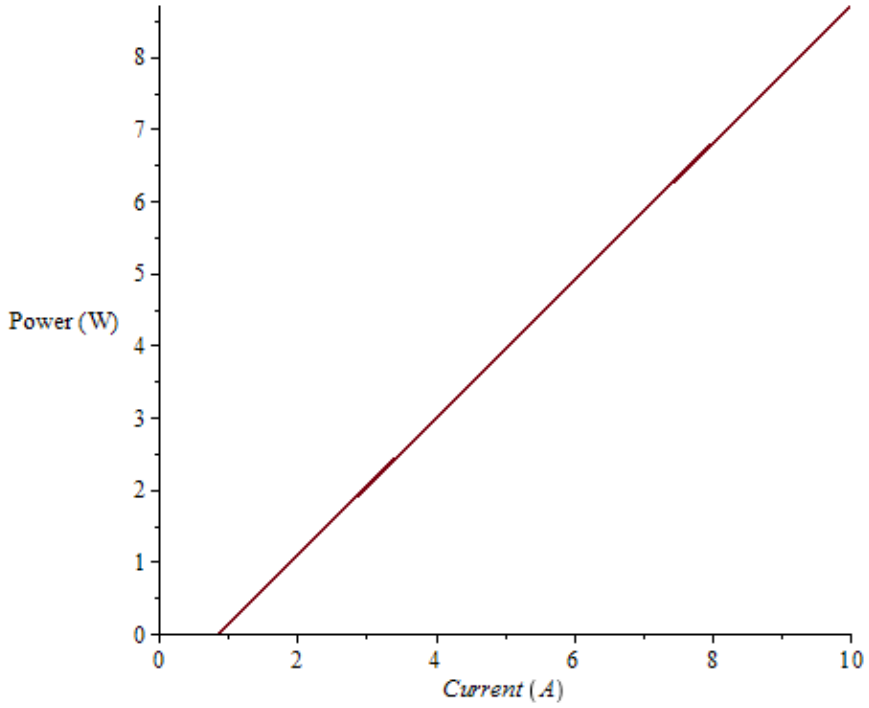

Figure 1.9: The calculated P-I characteristic of a 980 nm semiconductor laser

1.3 Longitudinal Spatial Hole Burning

In all types of semiconductor lasers, the lasing light intensity in the cavity is non-uniform along the laser axis. According to the rate equation (Equation 1.3), carrier density is related to the photon density. Specifically, the higher the photon density, the smaller the carrier density, and the smaller the optical gain. Therefore, longitudinal inhomogeneous light intensity leads to non-uniform distribution of carrier density, which in turn leads to non-uniform longitudinal optical gain. This effect is called longitudinal spatial hole burning (LSHB). In other words, under the effect of LSHB, for injection current beyond threshold, the local gain of semiconductor lasers is no longer simply saturated at a constant threshold value, and neither is the carrier density. This physical effect is not captured in the classic rate equations presented in 1.3 and 1.4, and an alternative physical description is required.

There are generally two kinds of LSHB. One is short-range LSHB, which is due to the standing wave pattern of laser modes, and the variation of carrier density is on the spatial scale of laser wavelength [14]. This effect is averaged out in lasers which operate on many longitudinal modes. The other is long-range LSHB, which is much stronger and becomes the focus of this thesis. This phenomenon can be easily understood through the following calculation. Assume the cavity length of a high-power semiconductor laser is 1 unit. The reflectivities of two facets, R_1 and R_2, are both 50%, the optical output power through R_1 is 10 Watts, and the internal loss of this semiconductor laser is ignored. In order to calculate the optical power inside cavity, the cavity length is discretized into 100 points. Following the propagation of laser light, the optical power at any point is related to that at the adjacent point as shown in Equation 1.15.

$$P_2 = P_1 \exp(\Delta z g_{th}) \tag{1.15}$$

Δz is mesh size, and L is overall cavity length. The initial power at R_1 facet can be determined by the output power. The optical power starts to accumulate as it propagates from R_1 to R_2 through gain medium. After being reflected 50% back by R_2, it turns round and propagates along the opposite direction. The total optical power inside the cavity is the sum of the power propagating forwards and backwards. Figure 1.10 shows the total power inside the cavity in longitudinal direction. As observed in Figure 1.10, although the threshold gain is assumed constant, the optical intensity is inhomogeneous along longitudinal position. The percentage variation can be calculated by Equation 1.16.

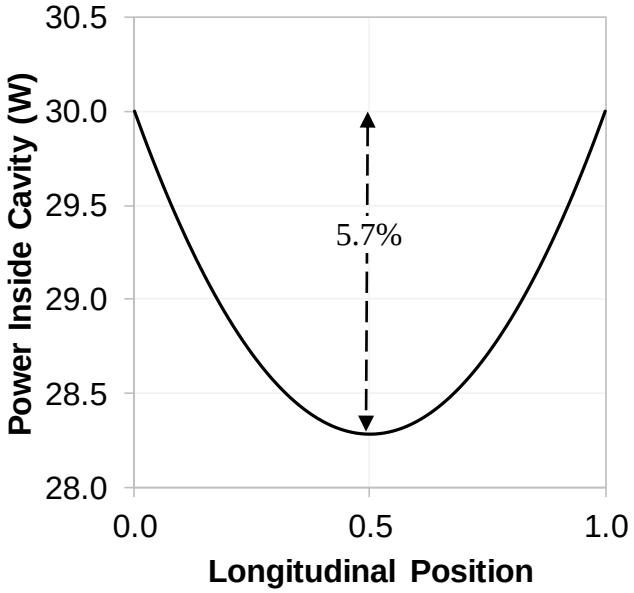

Figure 1.10: Power inside cavity in longitudinal direction (R_1=R_2=50%)

$$\%\, change = \frac{P_{max} - P_{min}}{P_{max}} \tag{1.16}$$

For practical application, the facets of high-power semiconductor lasers are usually coated with asymmetric reflectivities: one high-reflecting (HR) and one partial-reflecting (PR). This method is designed to improve slope efficiency and maximize output power in one direction [15]. However, asymmetric reflectivities lead to a more inhomogeneous light intensity distribution, and therefore stronger LSHB effect. The calculation of the aftermentioned semiconductor laser was modified with 20% PR and 100% HR. Figure 1.11 shows the power inside the cavity of this modified model.

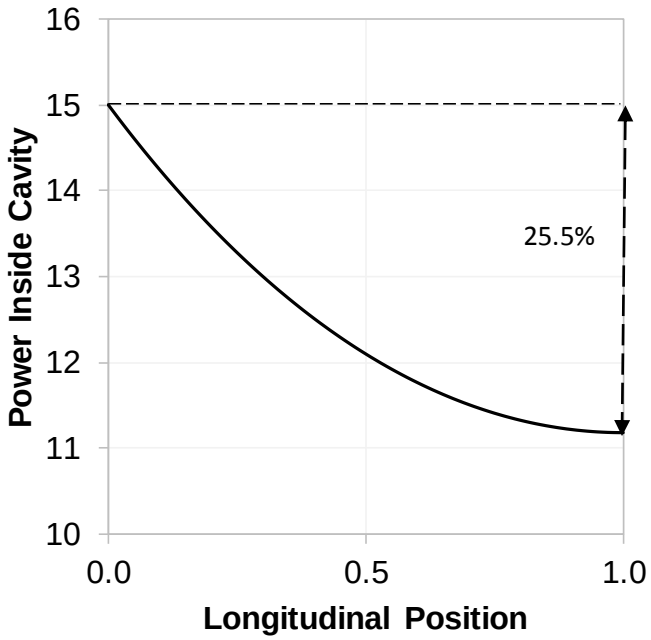

Figure 1.11: Power inside cavity in longitudinal direction (R_1=20%, R_2=100%)

The percentage variation of optical power inside the cavity is 25.5% for this asymmetric semiconductor laser, compared with 5.8% of the symmetric one. This variation is even larger for more highly asymmetric laser diodes. This strong inhomogeneous longitudinal photon distribution

leads to strong non-uniform longitudinal carrier density and optical gain, especially in high-power semiconductor lasers, motivating consideration of LSHB in such devices.

Further, recent effects to improve performance and reliability by reducing the junction temperature have led to semiconductor lasers with even longer cavity lengths, leading to even more inhomogeneous gain distributions. This effect will be further discussed in Chapter 3. To summarize, there are two major factors which lead to LSHB in high-power semiconductor lasers—asymmetric facet reflectivities and long cavity lengths.

Due to the non-uniform gain distribution, the LSHB effect is expected to limit the maximum achievable output power of high-power semiconductor lasers [16]. This imposes a limitation on increasing cavity length and asymmetric reflectivities. These spatial inhomogeneities also affect the nonlinearity and stability of a semiconductor laser [17]. Therefore, it is important to study in depth how LSHB affects the laser output.

In this thesis, an effective calculation model which can be used to analyze the impact of LSHB and applied to the design of high-power semiconductor laser designs is presented. The calculation model is based on a modified set of rate equations. The standard rate equations assume uniform longitudinal photon density, carrier density and optical gain, which is clearly not true. The rate equations must be modified to reflect spatially-varying characteristics along longitudinal direction, with local carrier density $N(z)$, local photon density $N_p(z)$, and local gain $g(z)$ varying with longitudinal position z. The working model is further discussed in Chapter 2.

1.4 Numerical Analysis

The inhomogeneous photon density distribution leads to non-uniform carrier density and gain, and in turn, this non-uniform gain acts on photon density. These three elements are closely coupled, making it difficult to analyze using simple analytic techniques. Therefore, the position-dependent, coupled differential rate equations must be solved using numerical analysis techniques. A variety of numerical calculation techniques such as Finite Difference Method (FDM), Finite Element Method (FEM), and Finite Integration Technique (FIT) [18] have been applied to nano-optical simulations. Among all these techniques, FDM is a basic one which is suitable for solving the coupled differential equations. The finite difference method relies on discretizing a function on a grid, and approximates the solutions to a differential equation by approximating the derivatives [19], as shown in Equation 1.17. Figure 1.12 shows a schematic diagram of finite difference method.

$$\frac{\partial u}{\partial x} \approx \frac{u_{i+1} - u_i}{\Delta x} \tag{1.17}$$

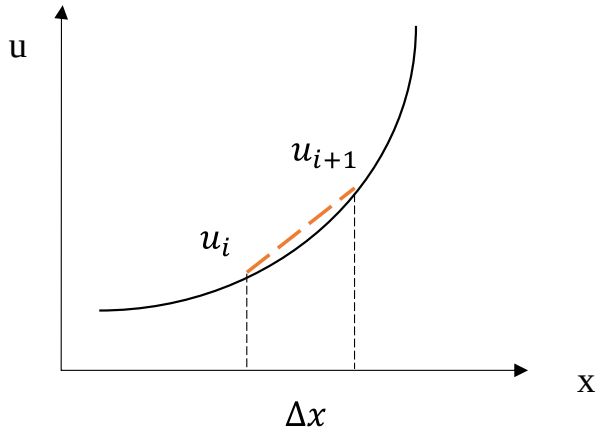

Figure 1.12: Schematic diagram of finite difference method

As a good example to illustrate how to use FDM in solving a practical problem, the one-dimensional heat equation was solved and the procedure is shown below. The problem is described in Figure 1.13. Assume a copper stick with length L is heated by a 1 Watt source Q at the center. This copper stick is a perfect heatsink and the temperatures at two ends are both 25˚C. The aim is to figure out the temperature distribution along the stick in steady state.

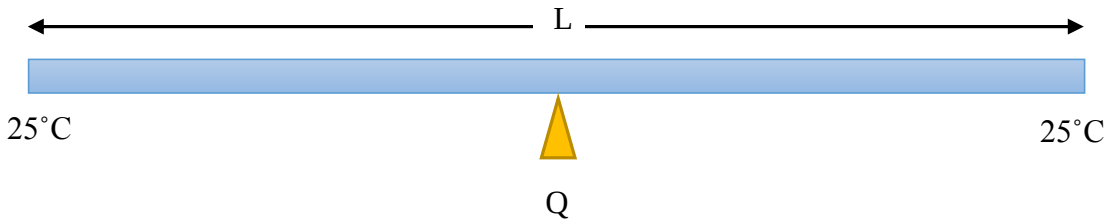

Figure 1.13: Schematic diagram of one-dimensional heat transfer problem

The general heat equation is shown in Equation 1.18, and it evolves into Equation 1.19 for steady state. T is defined as temperature; t is time; x is longitudinal position; α, C_p and ρ are heat transfer constants.

$$\frac{\partial T}{\partial t} - \alpha \frac{\partial^2 T}{\partial x^2} - \frac{Q}{C_p \rho} = 0 \tag{1.18}$$

$$\alpha \frac{\partial^2 T}{\partial x^2} + \frac{Q}{C_p \rho} = 0 \tag{1.19}$$

FDM is applied here to approximate the second-order derivative, shown in Equation 1.20.

$$\frac{\partial^2 T}{\partial x^2} = \frac{\partial}{\partial x}\left(\frac{\partial T}{\partial x}\right)$$

$$= \frac{\partial}{\partial x}\left(\frac{T_i - T_{i-1}}{\Delta x}\right)$$

$$= \frac{1}{\Delta x}\left(\frac{\partial T_i}{\partial x} - \frac{\partial T_{i-1}}{\partial x}\right)$$

$$= \frac{1}{\Delta x}\left(\frac{T_i - T_{i-1}}{\Delta x} - \frac{T_{i-1} - T_{i-2}}{\Delta x}\right)$$

$$= \frac{1}{\Delta x^2}\left(T_i - 2T_{i-1} + T_{i-2}\right) \tag{1.20}$$

By substituting Equation 1.20 into Equation 1.19, a finite difference heat equation is obtained.

$$T_{i+1} - 2T_i + T_{i-1} = \frac{-Q_i \Delta x^2}{c_p \rho \alpha} \tag{1.21}$$

The copper stick is simulated and divided into one hundred mesh size. At any longitudinal position, the temperature is determined by the values of its last and next position. To solve this finite difference equation, boundary condition is an important key, because it is used to set initial values and check if the calculation model is correct. The boundary condition of this problem is the fixed temperature at the two ends. Figure 1.14 shows the simulation result. For fixed boundary conditions T=25˚C, heat must uniformly diffuse in each direction so the temperature profile should be linear. The Matlab code is shown in Appendix B. Solving the position-dependent rate equations using FDM is similar as solving this heat transfer problem. The calculation will be discussed in depth in Chapter 2.

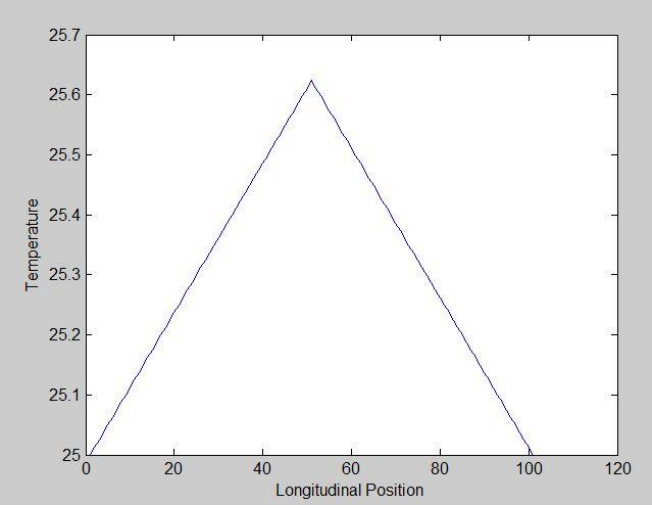

Figure 1.14: Simulation result of the one-dimensional heat transfer problem

1.5 Scope of Work

The LSHB effect has been investigated in several aspects in the history of semiconductor lasers. Some early previous work focused on LSHB in Fabry-Perot lasers, DFB lasers, and so on [20][21]. In this thesis, the LSHB effect in high-power edge-emitting semiconductor lasers was investigated theoretically and experimentally. In previous work, some of the calculation models were based on optical waveguide equations, and some were based on rate equations [16]. In this thesis, a self-consistent calculation model is built based on the modified rate equations, which more clearly presents the relation of photon density, carrier density, and optical gain. Compared with the different numerical analysis methods that were applied to solve the rate equations in previous work, such as FEM and the WIAS-TeSCA tool [22], FDM is used in this thesis to solve the differential rate equations, and Newton's method is applied to reduce residual error. Previously, most experimental work was carried out by scanning measurement of spontaneous emission through fiber and lens system [23]. In this thesis, the experimental verification of the calculation model was carried out by direct observation of spontaneous emission from a window patterned into the top contact of an 808 nm semiconductor laser.

Also, in this thesis, the impact of LSHB on output power is analyzed for different parameters, including injection current, cavity length, and wavelength. In prior work, the magnitude of LSHB was analyzed by formula approximation method [14]. Here, the direct analysis is performed based on the calculation result, which provides a more intuitive result. The analysis results are expected to be useful in the optimization of high-power semiconductor laser designs, considering the restriction of LSHB on asymmetric reflectivities and the increasing of cavity length of semiconductor lasers.

2. MODELING

2.1 Building the Model

A self-consistent calculation model incorporated LSHB was built based on modified rate equations. The modified spatially-varying rate equations for steady state are shown below [24]:

$$0 = \frac{\eta_i I}{qV} - \frac{N(z)}{\tau} - v_g g(z)[N_p^+(z) + N_p^-(z)] \tag{2.1}$$

$$\begin{pmatrix} \frac{dN_p^+(z)}{dz} = (\Gamma g(z) - \alpha_i) N_p^+(z) \\ \frac{dN_p^-(z)}{dz} = -(\Gamma g(z) - \alpha_i) N_p^-(z) \end{pmatrix} \tag{2.2}$$

Compared with the general rate equations shown as Equation 1.8 and 1.9, photon density, carrier density, and optical gain are modified to be position-dependent functions, instead of constants. Here N_p^+ and N_p^- are defined as forward and backward photon density respectively. Forward light propagates from PR facet (longitudinal position Z=0) to HR facet (longitudinal position Z=L), and the backward light propagates in opposite direction, shown in Figure 2.1.

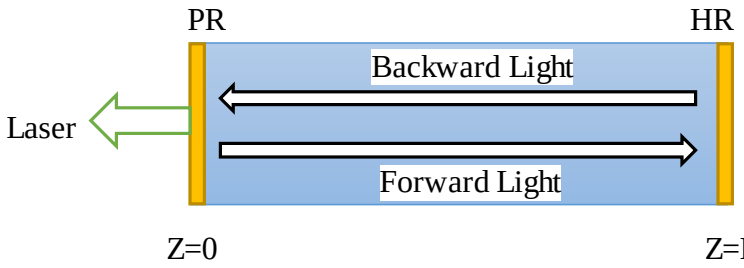

Figure 2.1: Schematic diagram of forward and backward propagating light

Unlike the carrier density or optical gain, the local photon density is different in opposite propagating directions because the gain is inhomogeneous. The forward light may experience a small local gain first and then a high local gain while the backward light experiences a high local gain first and then a small local gain. Therefore, the calculation of photon density must be separated into the calculations of $N_p^+(z)$ and $N_p^-(z)$. The total local gain $N_p(z)$ in the cavity is the sum of forward and backward photon density at position z.

$$N_p(\mathrm{z}) = N_p^+(\mathrm{z}) + N_p^-(z) \tag{2.3}$$

Equation 2.2 describes the increment of photon density in longitudinal direction. In this model, photon density loss is assumed mainly due to constant internal cavity loss α_i. Compared with the general rate Equation 1.9, the last term including photon lifetime is replaced by the internal loss. Therefore, the increment rate of photon density at position z is equal to the optical gain at position z minus the internal loss.

The reflection boundary conditions at two facets with reflectances R_{PR} and R_{HR} respectively, are shown in Equations 2.4 and 2.5. At the PR facet, the light traveling backwards is reflected a small part back into laser cavity, and continues traveling as forward light. Most of the backward light at PR facet contributes to laser output. At the HR facet, the light traveling forwards is reflected a large proportion back to laser cavity, and continues traveling as backward light.

$$N_p^+(0) = R_{PR} N_p^-(0) \tag{2.4}$$

$$N_p^-(L) = R_{HR} N_p^+(L) \tag{2.5}$$

The solutions to the modified rate equations combined with boundary conditions are shown to satisfy the threshold lasing condition [24] as Equation 2.6. The average model gain is equal to the threshold gain, which offset the mirror loss and internal loss. Also, Equation 2.6 evolves into the general threshold condition (Equation 1.14) when constant gain is assumed.

$$\frac{1}{L}\int_0^L \Gamma g(z) = g_{th} = \alpha_i + \alpha_m = \alpha_i + \frac{1}{2L}\ln(\frac{1}{R_{PR}R_{HR}}) \tag{2.6}$$

In order to obtain a numerical solution, the finite difference method introduced in Chapter 1 is employed here to solve this one-dimensional differential equation set. Equation 2.2 evolves into Equation 2.7 after approximating the derivative by finite difference equation, and dz is the grid length. Equation 2.7 shows the local photon density is determined by its previous value and the increment caused by the combined action of gain and loss. The key of this self-consistent calculation model is to solve the value of the first grid, defined as initial value, which is the value of the forward photon density at PR facet $N_p^+(z=0)$. Once this initial value is determined, the forward photon density along laser cavity can be calculated. According to the boundary condition at PR facet, $N_p^-(z=0)$ is related to $N_p^+(z=0)$, and then the backward photon density along laser cavity can be solved as well.

$$\begin{pmatrix} N_p^+(z+1) = N_p^+(z)[1 + dz(\Gamma g(z) - \alpha_i)] \\ N_p^-(z+1) = N_p^-(z)[1 - dz(\Gamma g(z) - \alpha_i)] \end{pmatrix} \tag{2.7}$$

The initial guess of $N_p^+(z=0)$ is based on the classic photon density solution introduced in Chapter 1. The boundary condition at HR facet is used to check and adjust the initial value, until

the residual error is close to zero. The residual error is defined as Equation 2.8, and it would approach to zero for exact solutions.

$$Residual\ error = \frac{R_{HR}N_p^+(L) - N_p^-(L)}{N_p^-(L)} \tag{2.8}$$

The calculation model is self-consistent, because Newton's method is employed here to adjust the initial value and reduce the residual error below 10^{-8}, which is small enough for good accuracy. Newton's method, also known as Newton–Raphson method, is usually applied to find successively better approximation to the roots of a real-valued function [25]. For one-variable function $f(x)$, it is usually implemented as Equation 2.9. x_n is an approximated root of $f(x)$, and a more accurate root $x_{n+1}$is found as follow:

$$x_{n+1} = x_n - \frac{f(x_n)}{f'(x_n)} \tag{2.9}$$

Combined with the finite difference method, Equation 2.9 can be rewritten as follow:

$$x_{n+1} = x_n - f(x_n)\frac{x_n - x_{n+1}}{f(x_n) - f(x_{n+1})} \tag{2.10}$$

In the LSHB calculation model, residual error is regarded as the one-variable function $Re(value)$, and the exact initial value is regarded as the root which makes the residual error to be zero, shown in Equation 2.10. $Value_2$ is more close to the exact value than $Value_1$, and Equation 2.11 will be iteratively until the residual error is small enough. Here Δ is the value difference applied in the finite difference method.

$$value_2 = value_1 - Re(value_1)\frac{-\Delta}{Re(value_1) - Re(value_1 + \Delta)} \tag{2.11}$$

This calculation model suits both the injection current below threshold and above threshold. When the injection current is below threshold, photon density N_p is set to be zero. For comparison, the situation without LSHB was also simulated. The calculation model is similar to the one with LSHB, except the gain and the carrier density are constant above threshold and clamped at g_{th} and N_{th}. Figure 2.2 and Figure 2.3 show the calculation flow chart for the model without LSHB and the model incorporated LSHB respectively. MATLAB code is shown in Appendix C.

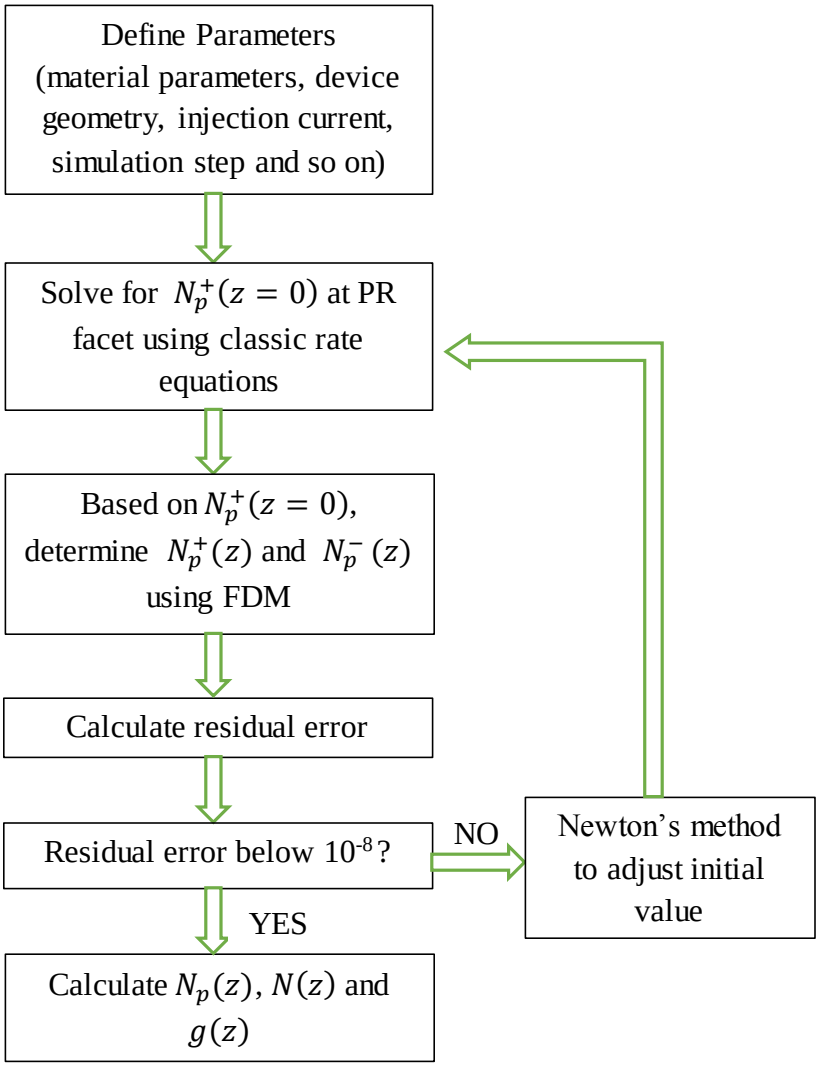

Figure 2.2: Calculation flow chart for the model without LSHB

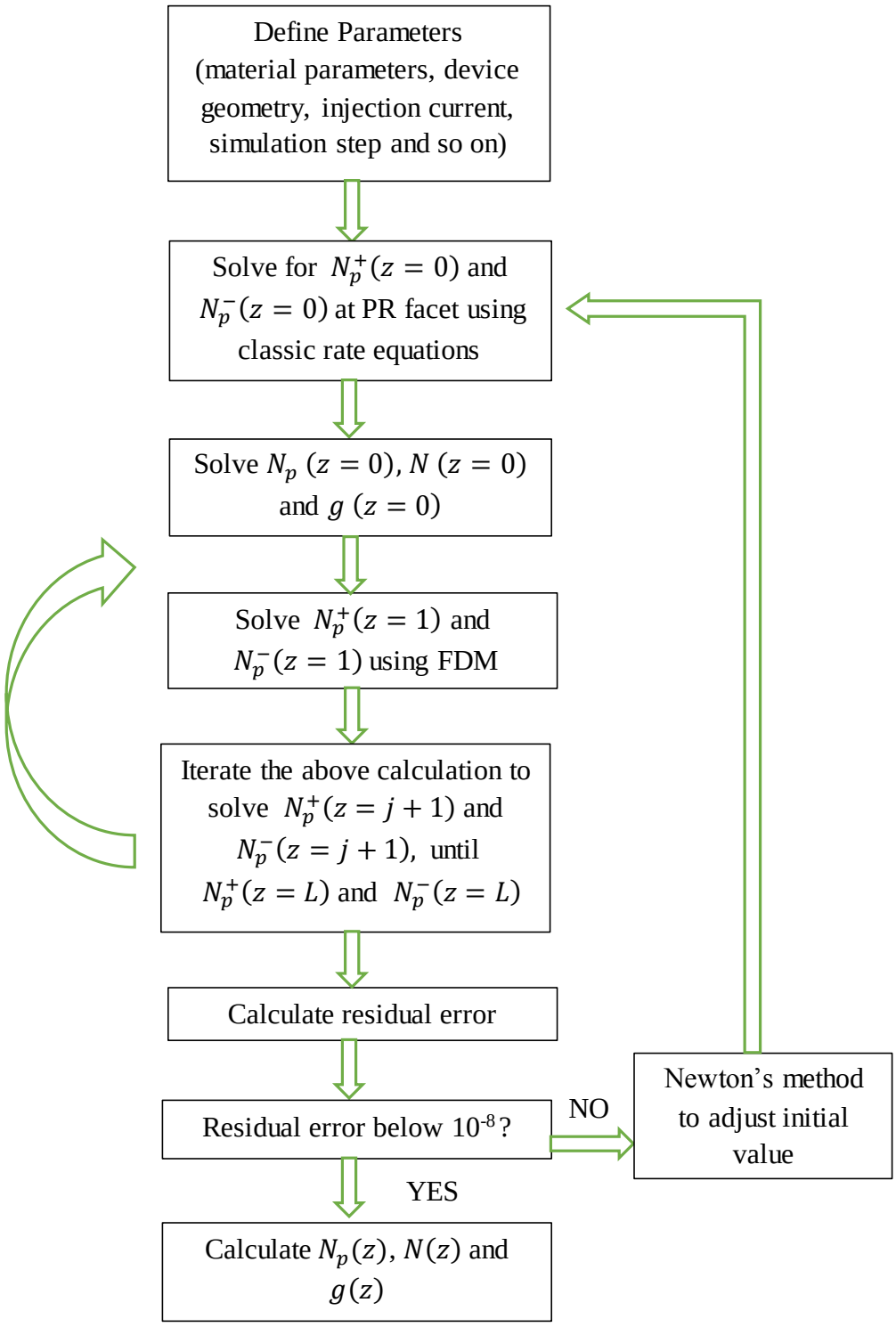

Figure 2.3: Calculation flow chart for the model with LSHB

2.2 Calculation Results

A 1475 nm InGaAsP high-power semiconductor laser was simulated, and the longitudinal photon density, carrier density, and optical gain were calculated with LSHB. The results without LSHB were also obtained for comparison. Table 2.1 shows the device parameters.

Table 2.1: Material and device parameters for the modeling semiconductor laser

Cavity length (μm)	3800	Internal quantum efficiency η_i	0.87
Quantum well thickness (Å)	140	Optical mode Γ	0.01
Emitter width (μm)	150	Internal loss α_i (1/cm)	2.0
HR	0.99	Refractive index	3.5
PR	0.005	g_0 (1/cm)	1000
J_{tr} (A/cm^2)	121	Threshold current I_{th} (A)	1.67
N_{tr} (1/cm^3)	1.1×10^{18}	Thermal resistance R_{th} (K/W)	2.2
T_0 (K)	50	T_1 (K)	150
σ (Ωcm^2)	7.8×10^{-5}	V_s (V)	22×10^{-3}
Spontaneous coefficient B (cm^6/s)	1×10^{-9}	Auger coefficient C (cm^9/s)	1×10^{-30}

Figure 2.4 shows the calculation results of forward and backward local photon densities with LSHB for an example injection current (I=5A). The forward photon density increases along longitudinal direction as it goes through gain medium. At the HR facet, 99% of the forward photon density is reflected as the initial value of backward photon density. This 99% reflection is guaranteed by the residual error below 10^{-8}. Then the backward photon density increases as it goes through the gain medium backwards. At the PR facet, 0.5% of the backward photon density is reflected as the initial value of forward photon density. This 0.5% reflection is guaranteed by the boundary condition at PR facet. The total photon density is the sum of backward and forward photon densities.

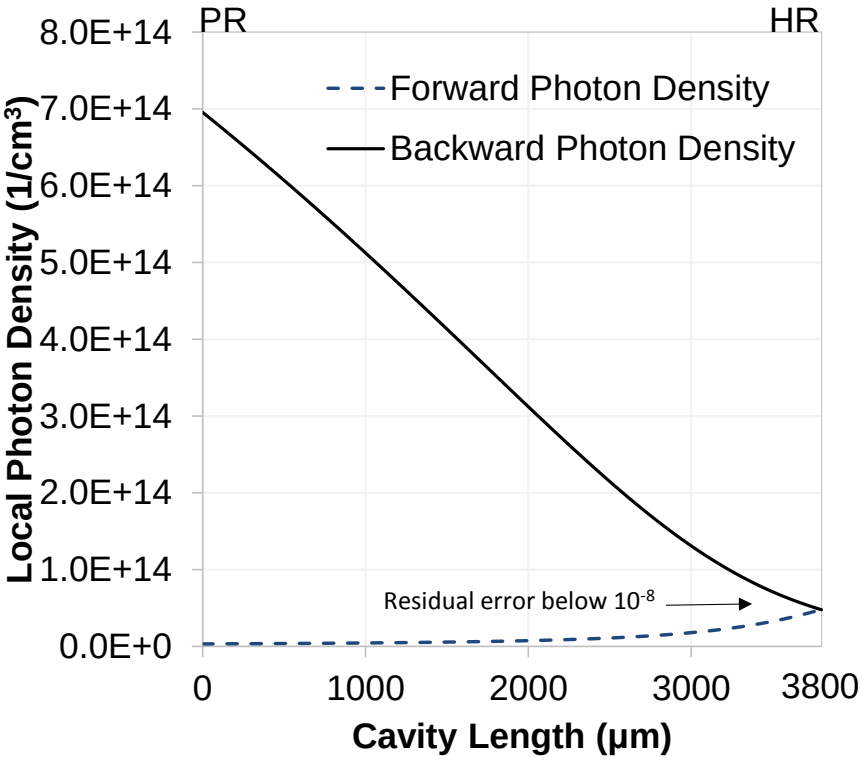

Figure 2.4: Calculation results of forward and backward local photon density with LSHB

Figure 2.5 compares the forward photon density with LSHB and the one without LSHB for the example injection current (I=5A). At the front part of laser cavity, the forward photon density with LSHB increases slowly compared to that without LSHB. At the back part of laser cavity, the rate of increase of the forward photon density with LSHB starts to exceed the rate without LSHB. The behavior of longitudinal photon density indicates the longitudinal distribution of optical gain. For the situation without LSHB, the photon density experiences a constant threshold gain in longitudinal direction. The smaller rate of increase of forward photon density with LSHB near PR facet is due to the smaller optical gain below threshold, while the optical gain becomes above threshold near HR facet which leads to a larger rate of increase than that without LSHB.

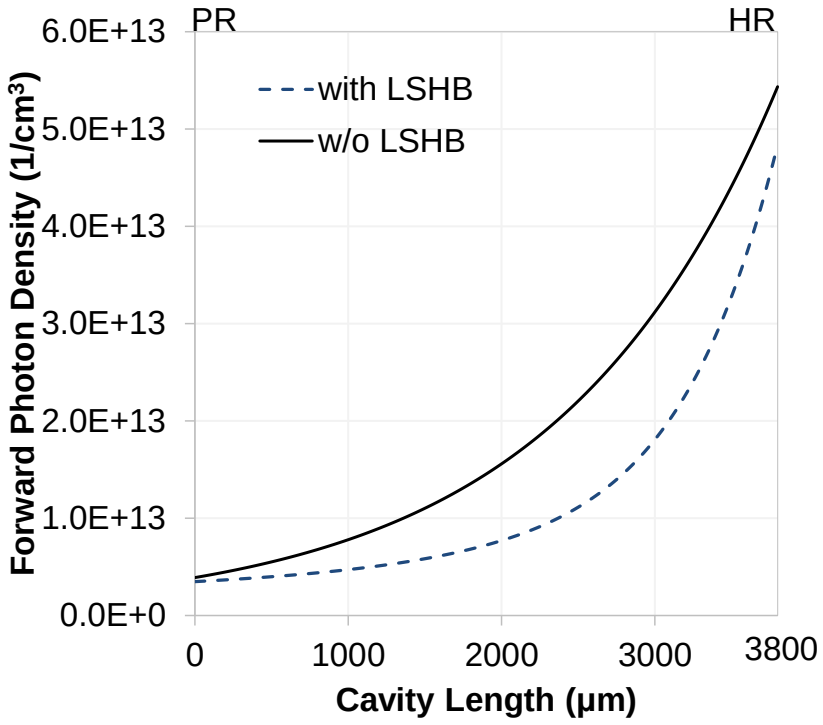

Figure 2.5: Comparison of forward photon density with LSHB & without LSHB

Figure 2.6 compares the backward photon density with LSHB and the one without LSHB for the example injection current (I=5A). The result can be explained similar to that of forward photon density. Following the light propagating backwards, first, the backward photon density with LSHB experiences a faster rate of increase than that without LSHB due to the higher optical gain above threshold near HR facet. Then the situation becomes reversed due to the optical gain below threshold near PR facet. As observed in Figure 2.6, the backward photon density without LSHB finally exceeds the one with LSHB at PR facet, which is related to the output power. Instead, in the center of laser cavity, the backward photon density with LSHB is higher due to the higher gain it experiences first. Since the backward photon density is much higher than forward photon density, the total photon density, which will be shown later, almost follows the shape of backward photon density.

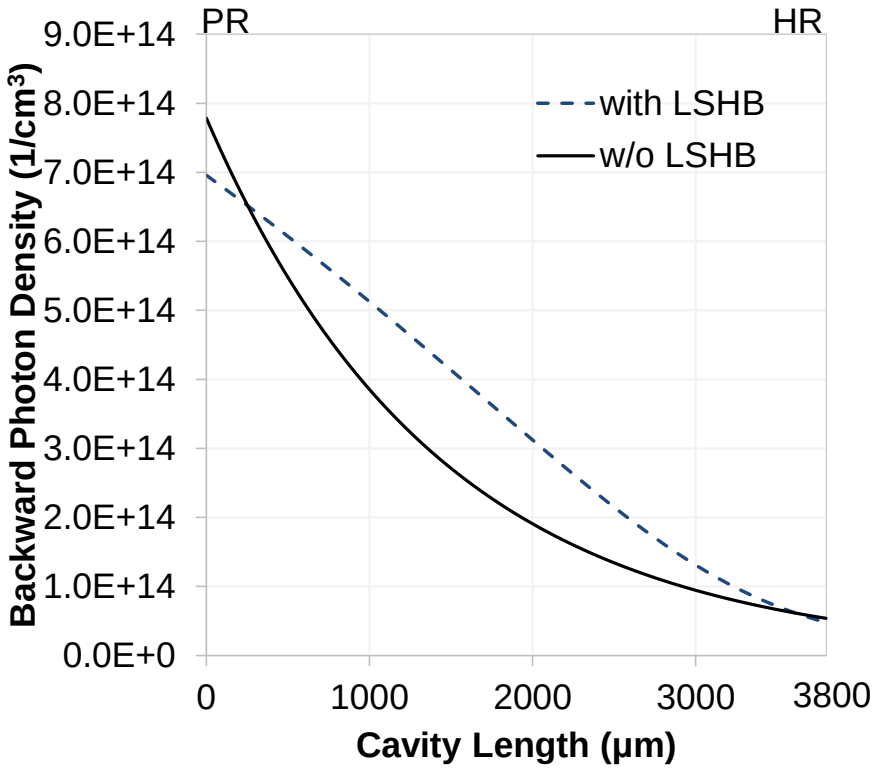

Figure 2.6: Comparison of backward photon density with LSHB & without LSHB

Figure 2.7 shows the calculated results of the non-uniform longitudinal photon density profiles at several injection currents. For comparison, the longitudinal profiles without LSHB are also plotted (dash line). As observed in Figure 2.7, the profiles with LSHB deviated more from those without LSHB when injection current increases, which indicates the gain profile is more inhomogeneous with increasing current. The photon density distribution with LSHB is reduced near the PR facet, which leads to a lower output power than the situation without LSHB. The relation of this reduced power with increasing current will be further discussed in Chapter 3.

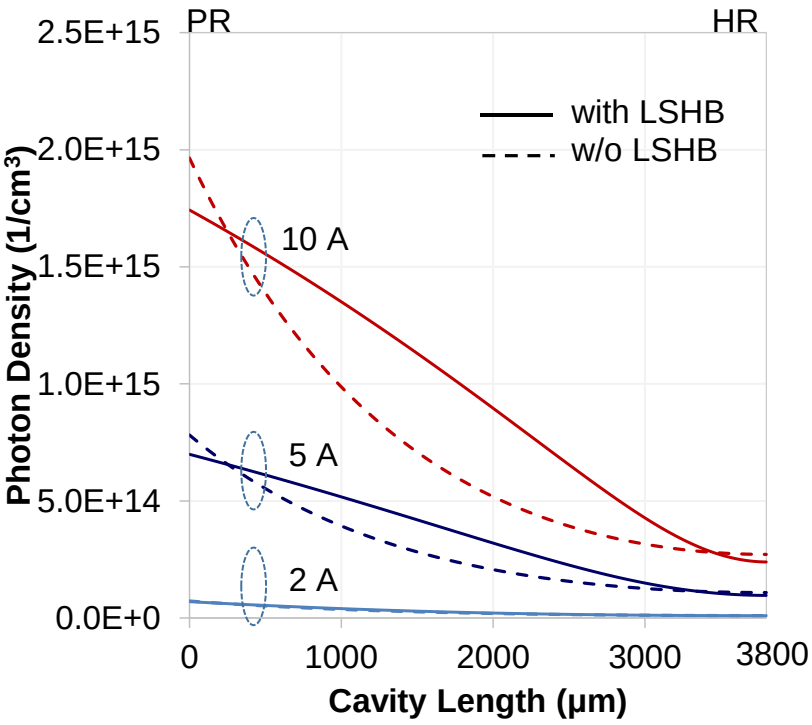

Figure 2.7: Calculation results of longitudinal profiles of photon density

Figure 2.8 shows the calculated longitudinal profiles of carrier density at several injection currents above threshold. Without LSHB, the carrier density (black line) is clamped at a constant threshold value along longitudinal position for any current above threshold. With LSHB, the distribution is smaller than the threshold value near the PR facet while it is larger than the threshold value near the HR facet. The non-uniformity becomes more obvious with higher applied current, which demonstrates that the impact of LSHB becomes greater with higher injection current in high-power semiconductor lasers. Also, this non-uniformity of LSHB is reflected in the point of intersection with threshold value. Increasing injection current causes the point of intersection to move towards the HR facet.

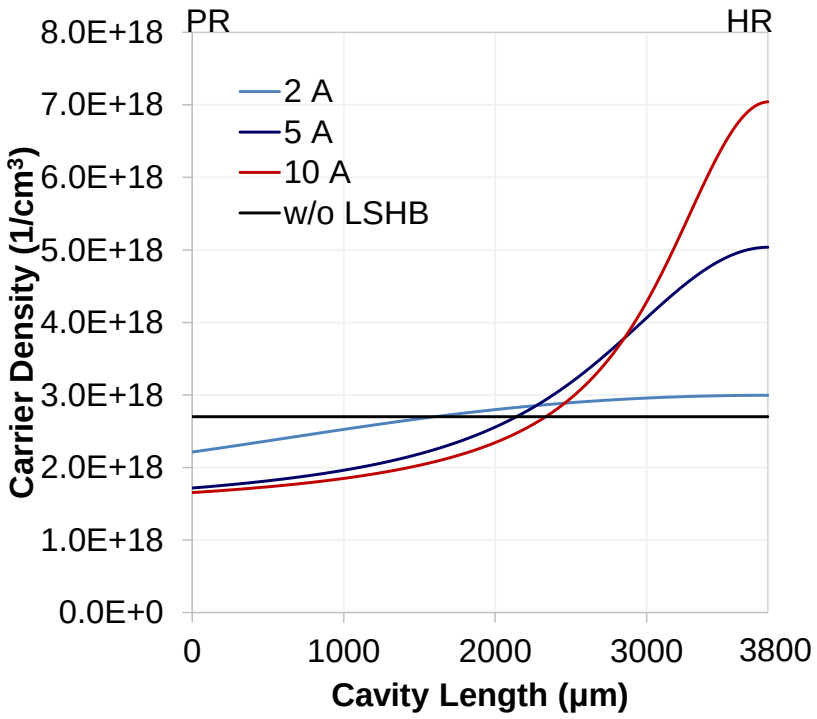

Figure 2.8: Calculation results of longitudinal profiles of carrier density

Figure 2.9 shows the calculated longitudinal gain distribution at several injection currents above threshold. Without LSHB, the optical gain is clamped at a constant threshold value along longitudinal position (black line). With LSHB, the non-uniform distribution is smaller than the threshold value near the PR facet while it is larger than the threshold value near the HR facet. Compared with the profiles of photon density, the gain saturation effect is demonstrated. The higher the local photon density, the smaller the local carrier density and gain. Also, the calculated average gain with LSHB in longitudinal direction is equal to the threshold gain, which satisfies the threshold lasing condition as indicated in Equation 2.6 in Chapter 2.1.

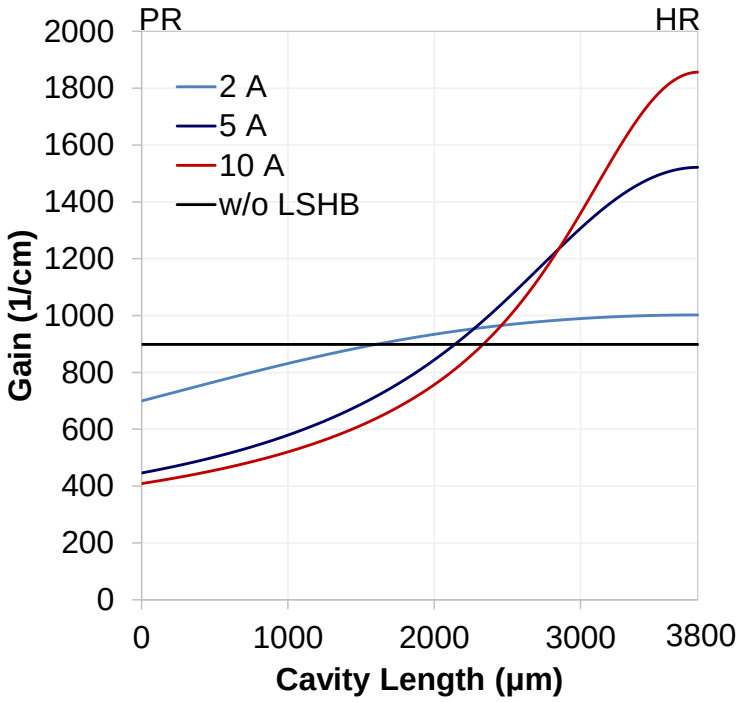

Figure 2.9: Calculation results of longitudinal profiles of optical gain

Based on the distribution of photon density, the output optical power can be calculated as follows:

$$P_{output} = dw\frac{hc}{\lambda\Gamma}v_g\left[N^-_{p\,z=0}(1-R_{PR}) + N^+_{p\,z=L}(1-R_{HR})\right] \tag{2.12}$$

The output power is determined by the forward propagating photons coming out at the HR facet and the backward propagating photons coming out at the PR facet. Here d and w are the quantum well thickness and emitter width respectively, h is Plank's constant, c is the velocity of light in vacuum, and R_{PR} and R_{HR} are the facet reflectivities. Power conversion efficiency, also known as wall-plug efficiency, is another important index to evaluate the quality of a high-power semiconductor laser. It is the ratio of input electrical power by output optical power, shown in Equation 2.13. The input power is calculated as Equation 2.14.

$$Wallplug\ Efficiency = \frac{P_{output}}{P_{input}} 100\% \tag{2.13}$$

$$P_{input} = I \times V \tag{2.14}$$

The input power is determined by the product of injection current and the total voltage across the diode's terminals. Figure 2.10 shows the comparison of output power and wall-plug efficiency for both the situations with LSHB and without LSHB. As observed in Figure 2.10, LSHB suppresses the output power as expected mainly due to the reduction of photon density at the PR facet. Also, LSHB decreases the power efficiency by nearly 5% for this specific 1475 nm high-power semiconductor laser. The impact of LSHB with increasing current will be discussed in next chapter.

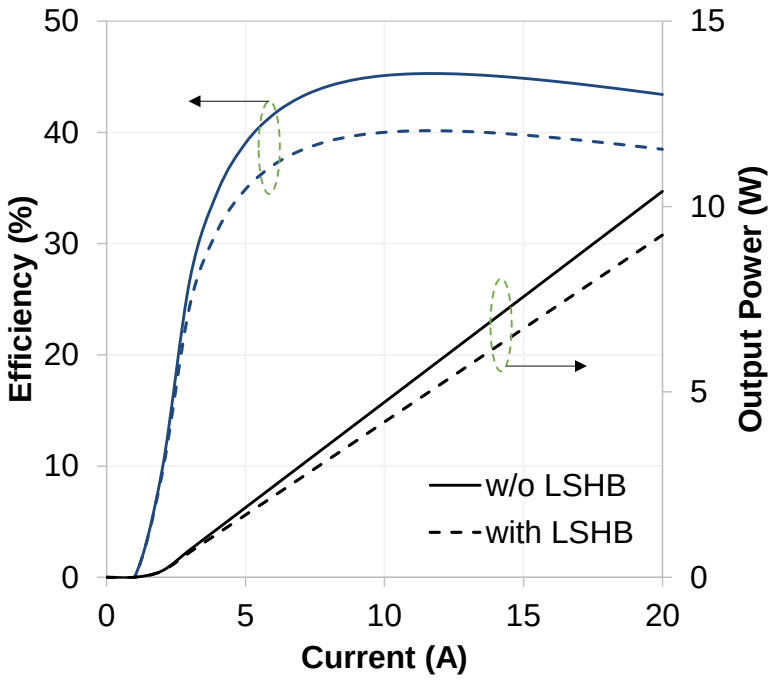

Figure 2.10: Comparison of power and efficiency with LSHB & without LSHB

3. ANALYSIS

3.1 The Impact of LSHB with Increasing Injection Current

According to the simulation results in Chapter 2, the non-uniformity of gain, and hence LSHB, become greater with increasing injection current. For high-power semiconductor lasers, the output power is the most important factor to be considered, so we are interested in whether this aggravating LSHB effect with increasing current will cause the output power to change significantly. As mentioned before, the photon densities near PR and HR facets are suppressed due to LSHB, and the reduction of output optical power can be calculated with the photon densities at the facets. Therefore, based on the calculation model, the impact of LSHB on output power with increasing current can be analyzed.

As we know, besides LSHB, self-heating is another important factor that cannot be ignored when analyzing the power output of high-power semiconductor lasers. Therefore, at this point, thermal effects are incorporated into the calculation model. As introduced in Chapter 1, the output power can be determined as Equation 1.1 with differential quantum efficiency η_d and threshold current I_{th}. The output power under thermal effects is calculated by imposing additional exponential dependence of I_{th} and η_d with thermal resistance R_{th} and characteristic temperatures T_0 and T_1, shown in Equation 3.1 through Equation 3.5 [26]. Thermal resistance is a parameter having units [K/W] which quantifies the material resistance to heat flow [27]. Also, the thermal resistance is inversely proportional to the length and width of the laser cavity [28]. Figure 3.1 shows a schematic diagram of a temperature rise due to thermal resistance.

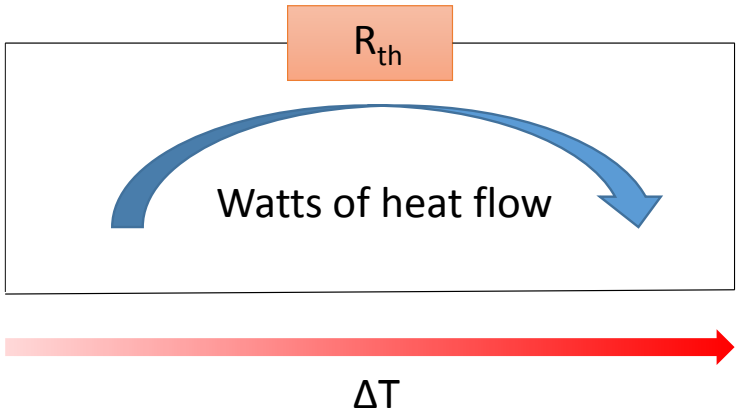

Figure 3.1: Schematic diagram of a temperature rise due to thermal resistance

In semiconductor lasers, as shown in Equation 3.5, waste heat ($P_{input} - P_{output}$) drives temperature rise. Equation 3.2 and 3.3 describe the exponential increase of threshold current and the exponential decrease of differential quantum efficiency with increasing temperature. The characteristic temperatures T_0 and T_1 stand for the rate of variation, the smaller the characteristic temperatures, the faster the change.

$$P_{thermal} = \eta_{d\_thermal} \frac{hc}{\lambda q} \left(I - I_{th\_thermal}\right) \tag{3.1}$$

$$I_{th\_thermal} = I_{th} e^{\frac{\Delta T}{T_0}} \tag{3.2}$$

$$\eta_{d\_thermal} = \eta_d e^{\frac{-\Delta T}{T_1}} \tag{3.3}$$

$$\eta_d = \frac{\eta_i \alpha_m}{\alpha_i + \alpha_m} \tag{3.4}$$

$$\Delta T = R_{th}\left(P_{input} - P_{output}\right) \tag{3.5}$$

Figure 3.2 shows the comparison of calculated output powers under four different sets of conditions with injection current ranging from 2A to 40A ($I_{th} = 1.7A$). As observed in Figure 3.2, LSHB suppresses the output power in both situations no matter whether thermal effect is considered or not. Also, LSHB shifts the rollover point of output power under thermal effect towards low current. This is because the power reduced by LSHB further drives the waste heat ($P_{input} - P_{output}$). According to Equation 3.5, this increased waste heat leads to a larger ΔT than the one without LSHB. A larger temperature rise results in further suppression of output power, and the rollover point shifts towards lower injection current, as illustrated in Figure 3.3 [29].

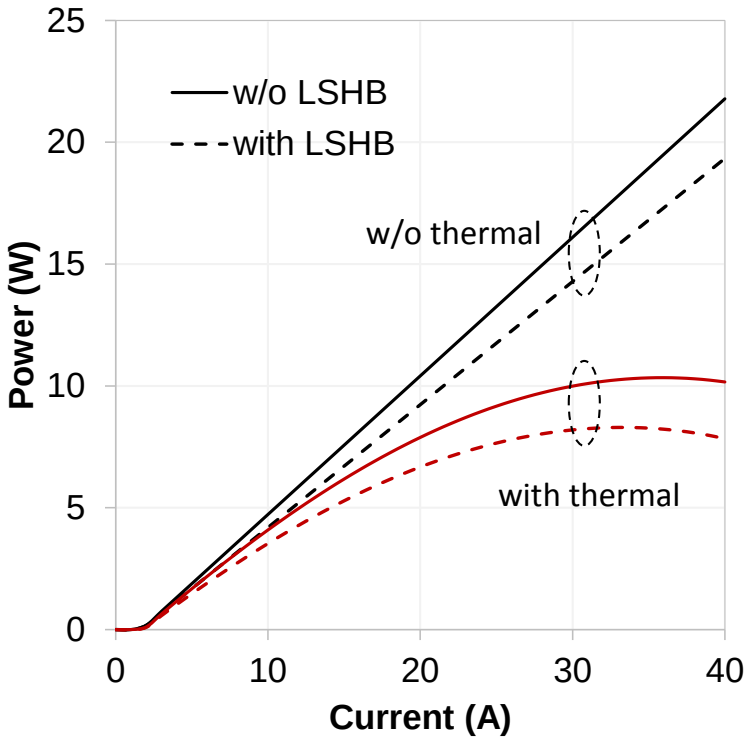

Figure 3.2: Comparison of calculated output powers with increasing current

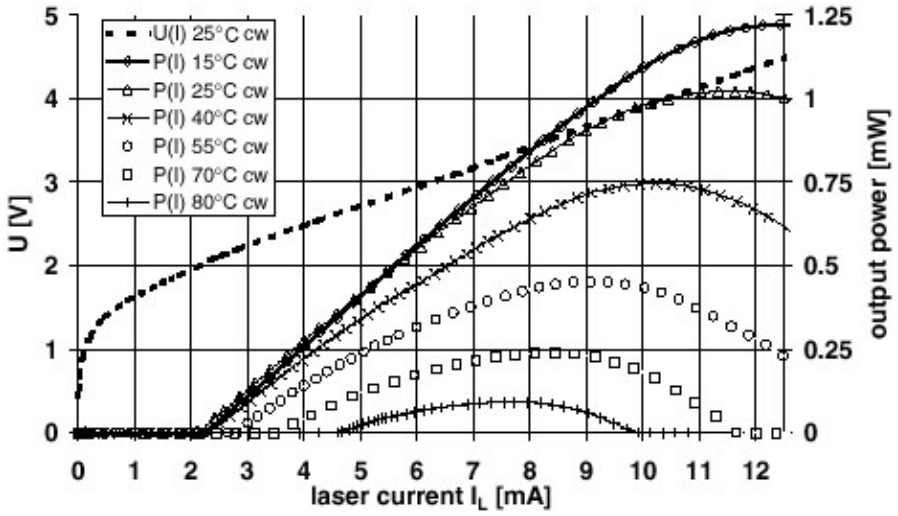

Figure 3.3 P-I-V characteristics at several different heatsink temperatures [29]

In order to analyze the magnitude of the impact of LSHB on output power and whether it changes with increasing current, the percentage power difference was calculated and the result is shown in Figure 3.4 with injection current from 2A to 20A ($I_{th} = 1.7A$).

$$\%\ Difference = \frac{P_{w/o\ LSHB} - P_{with\ LSHB}}{P_{w/o\ LSHB}} \tag{3.6}$$

As observed in Figure 3.4, when thermal effects are not considered, below a certain current value (around 5A for this specific 1475nm laser diode), the percentage power difference gets larger with increased current and then reaches an approximated steady value (11% in this case). This is because by this point, the injection current is high enough to make the non-stimulated recombination term $\frac{N(z)}{\tau}$ in the rate equations to become fairly small compared to the other terms related to current and photon density. In [14], Ryvkin and Avrutin state that in the calculation of LSHB with high injection current, this term can be omitted, and therefore they conclude that the non-uniform carrier density distribution does not depend on the pumping current. The calculated profiles of carrier density and gain in Chapter 2 also corroborate this claim. The difference of

carrier density at PR facet between 5A and 10A is really small compared to the difference between 2A and 5A, and so is the optical gain. This is the reason why the impact of LSHB on output power increases quickly at first, but eventually tends to saturation.

However, this work shows that the conclusion is different when self-heating is considered. As the injection current goes up, the percentage power difference increases continuously, which indicates the impact of LSHB on output power becomes larger with increasing current. For this specific laser, ~15% power suppression occurs around 20A due to LSHB. When self-heating is considered, LSHB not only reduces the output power by the suppression of the photon density at the facets, it also contributes to the temperature rise which further erodes output power.

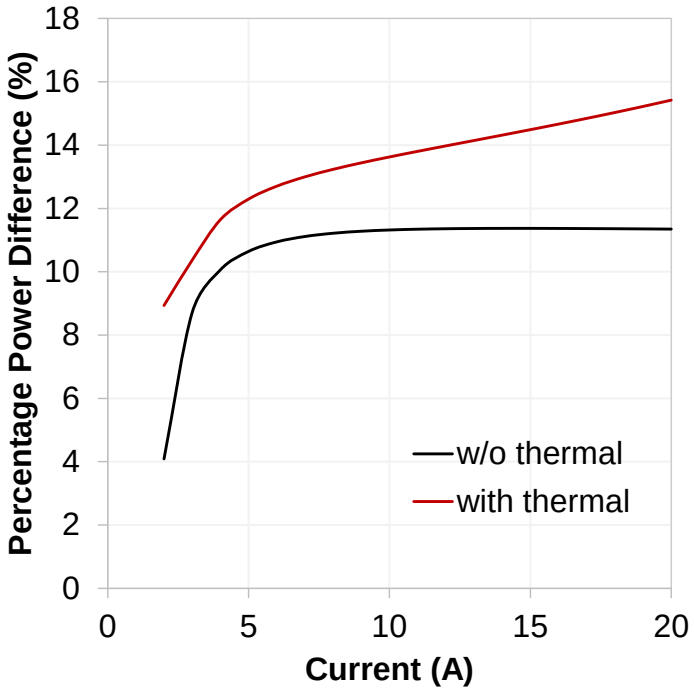

Figure 3.4: Percentage power difference due to LSHB with increasing current

3.2 The Impact of LSHB with Increasing Cavity Length

The cavity lengths of commercial high-power semiconductor lasers have been progressively increased to better distribute heat and improve output power. Therefore, it is important to investigate whether the impact of LSHB on output power will change with increasing cavity length. Since the input powers (for equivalent output) are different for various cavity lengths (Equation 3.4), wall-plug efficiency was analyzed instead of output power.

In order to make the cavity length a single variable, mirror loss was kept constant by adjusting the low reflectivity R_{PR} according to Equation 3.7. The reason for this is in practice, as cavity length is changed, the mirror loss is adjusted to maximize the operating slope efficiency.

$$\alpha_m = \frac{1}{2L} \times ln\left(\frac{1}{R_{PR} \cdot R_{HR}}\right) \tag{3.7}$$

Thermal resistance R_{th} was also adjusted to correct for length variation. Another issue requiring consideration is that for different injection currents, power efficiency is not constant [30]. Therefore, peak power efficiencies are compared for different cavity lengths. The result is shown in Figure 3.5. As observed in Figure 3.5, without LSHB, for this specific 1475nm semiconductor lasers, there is almost no change in peak power efficiency with the increasing cavity length, regardless of whether thermal effect is considered or not. However, with LSHB, peak power efficiency decreases as the cavity length increases. That means the impact of LSHB becomes greater with the increase of cavity length.

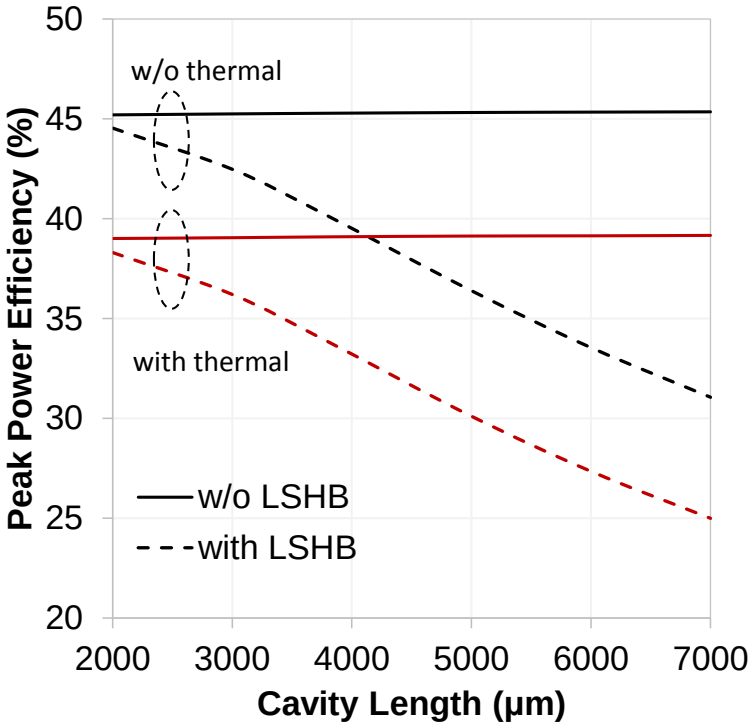

Figure 3.5: The impact of LSHB on peak power efficiency with increasing cavity length

In order to understand the origin of this result, the impact of LSHB on output power with increasing cavity length was also calculated by making the reflectivities of the two facets identical. As the cavity length increases, the reflectivities were kept the same with each other to keep a constant mirror loss. Figure 3.6 shows the calculation result in this case. As observed in Figure 3.6, there is no difference of the impact of LSHB on output power with increased cavity lengths. That means the increasing impact of LSHB on output power with increased cavity length is acted through the decrease of partial reflectivity. As shown in Equation 3.7, longer cavity length requires smaller partial reflectivity to keep the mirror loss constant and obtain the optimum output. The smaller partial reflectivity makes the semiconductor laser more asymmetric, which leads to further aggravation of the LSHB effect.

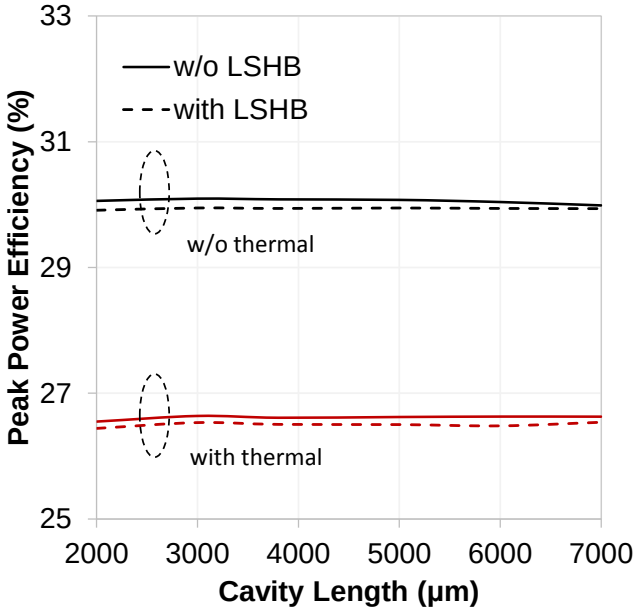

Figure 3.6: Peak power efficiency with increasing cavity length for identical reflectivities

To measure the impact of LSHB with increased cavity length, the percentage difference of peak power efficiency (% change in $\eta_{wp,\,peak}$) was calculated and the result is shown in Figure 3.7.

$$\%\,Difference = \frac{\eta_{wp,peak\,w/o\,LSHB} - \eta_{wp,peak\,with\,LSHB}}{\eta_{wp,peak\,w/o\,LSHB}} \tag{3.8}$$

As observed in Figure 3.7, for this specific 1475nm semiconductor laser, without thermal effect, the percentage difference of peak power efficiency due to LSHB increases by 6% per 1000μm length, and it is beyond 10% at around 3600μm cavity length. With thermal effect, the percentage difference of peak power efficiency increases by 6.9% per 1000μm length, and it is beyond 10% at around 3400μm cavity length. The different percentage is because the original output power under thermal effects is small. Therefore, for the same power reduction caused by increased cavity length, the percentage difference is bigger for the case with thermal effects.

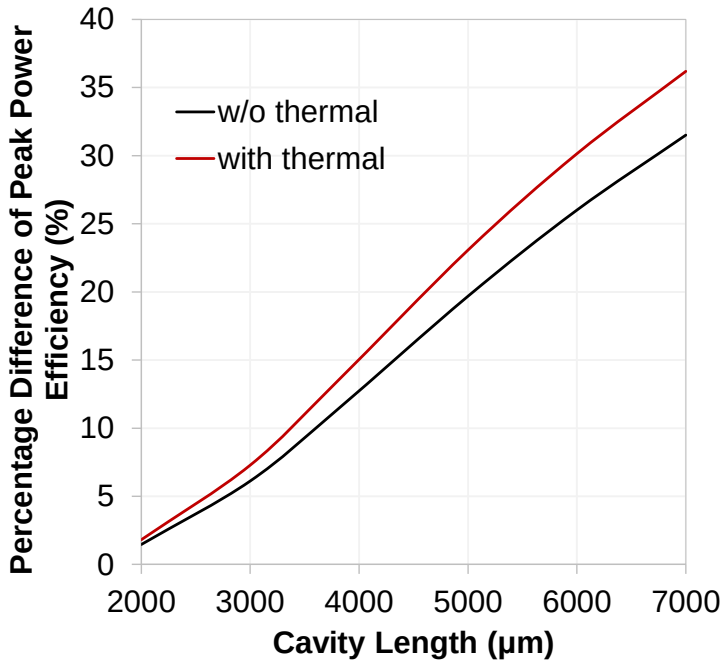

Figure 3.7: Percentage difference of peak power efficiency with increasing cavity length

3.3 The Impact of LSHB with Varying Wavelengths

High-power semiconductor lasers of different wavelengths are designed to meet the needs of various applications. According to the calculation equations of input and output powers for high-power semiconductor lasers, lasers with shorter wavelength can operate with higher input and output powers. Figure 3.8 shows the comparison of power conversion efficiency for different wavelengths based on the calculation model without thermal effects. The observed higher power efficiency in shorter wavelengths is typical of commercial devices [31].

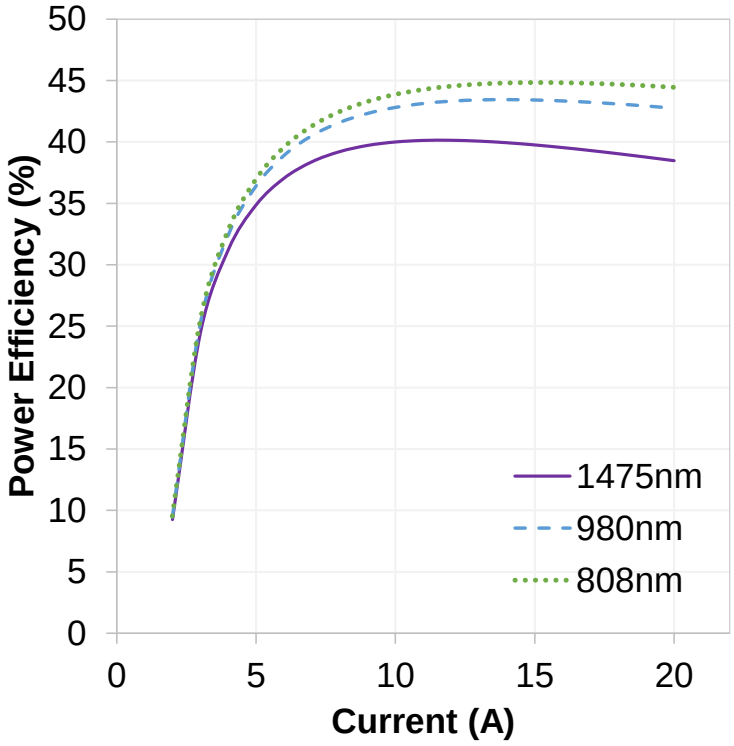

Figure 3.8: Comparison of power efficiencies for different wavelengths

In order to investigate the impact of LSHB for different wavelengths, the percentage power difference (Equation 3.6) for three different wavelengths, 808nm, 980nm, and 1475nm, were calculated and compared. The result is shown in Figure 3.9.

As observed in Figure 3.9, without thermal effect, the impacts of LSHB are the same for these three different wavelengths. The percentage power differences all climb to a steady value beyond certain injection current, which is exactly the same conclusion made in Chapter 3.1. However, with self-heating, one can conclude that the semiconductor lasers with shorter wavelength are more greatly affected by LSHB.

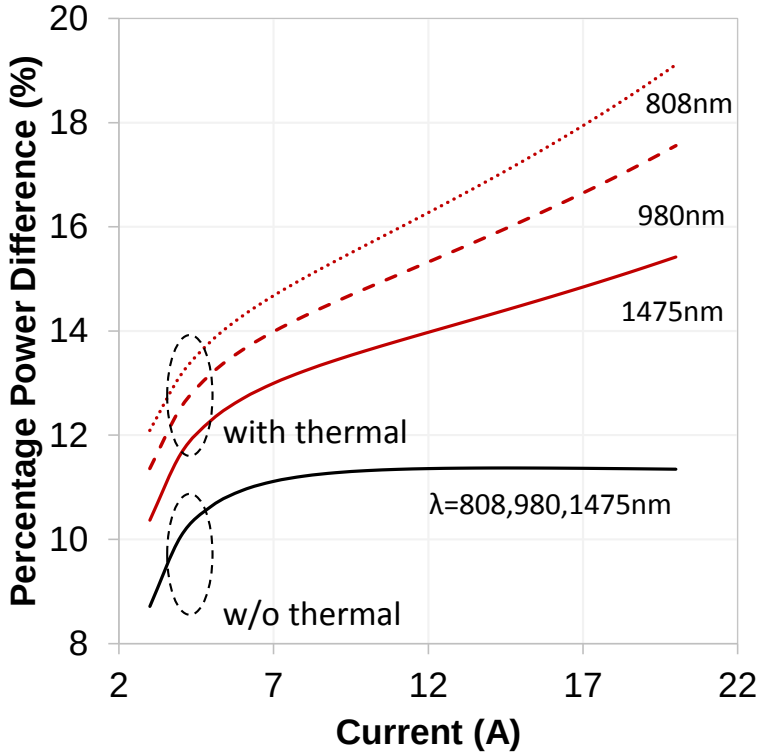

Figure 3.9: Comparison of percentage power difference for different wavelengths

The reason can also be explained by the temperature rise ΔT caused by LSHB. Since the laser with shorter wavelength has higher output power, and the percentage power differences due to LSHB without thermal effects are the same for all the wavelengths. Therefore, the power reduced by LSHB is larger for the shorter wavelength, which leads to a larger waste power and causes a higher temperature rise. As mentioned before, higher temperature rise results in more power suppression that makes a bigger percentage power difference for the shorter wavelength semiconductor laser under thermal effects.

4. EXPERIMENT

4.1 Laser Safety

The output powers of high-power semiconductor lasers can be several watts or even more, and they emit infrared light which is invisible to human eyes. Therefore, the laser safety for conducting experiments with high-power semiconductor lasers is significant.

First, direct observing the laser light can cause blindness. At high powers, even scattered light caused by specular reflection at a surface is sufficient to cause damage. For each laser in use, we are interested in identifying the maximum safe energy that may be incident upon the eyes. This is evaluated by Maximum Permissible Exposure (MPE). The MPE is usually expressed in terms of the allowable exposure time (in seconds) for a given irradiance (in watts/cm^2) at a particular wavelength [32]. This is the minimum irradiance or radiant exposure that may be incident upon eyes (or skin) without causing biological damage. The basic method for evaluating the safety of a specific laser system is to calculate the maximum irradiance that an unprotected eye might experience while the laser system is operating, and check whether it is less than the MPE. The values of MPE for selected lasers of different wavelengths can be found in [32].

To protect against the laser exposure above MPE, safety goggles (with highly absorbing lenses) are used for protection. The chosen goggles must be above the minimum optical density (OD) associated with the type and power of laser. The minimum OD is dependent on wavelength and output power of lasers because the absorptive properties of the eye tissues vary with wavelength. The Laser Institute of America (LIA) maintains an online tool to simply calculate what OD is recommended for use with a laser system with a given power [33]. Figure 4.1 shows

the minimum OD requirement for power ranging from 1mW to 1kW in 10x steps (dotted lines) for the wavelength ranging from 750 nm to 2100 nm. The plot also shows the OD specifications for an example Thorlabs LG11 goggle (solid line) [34]. As observed in Figure 4.1, the OD specification of the example goggle is above the minimum OD requirement in most wavelength and power range.

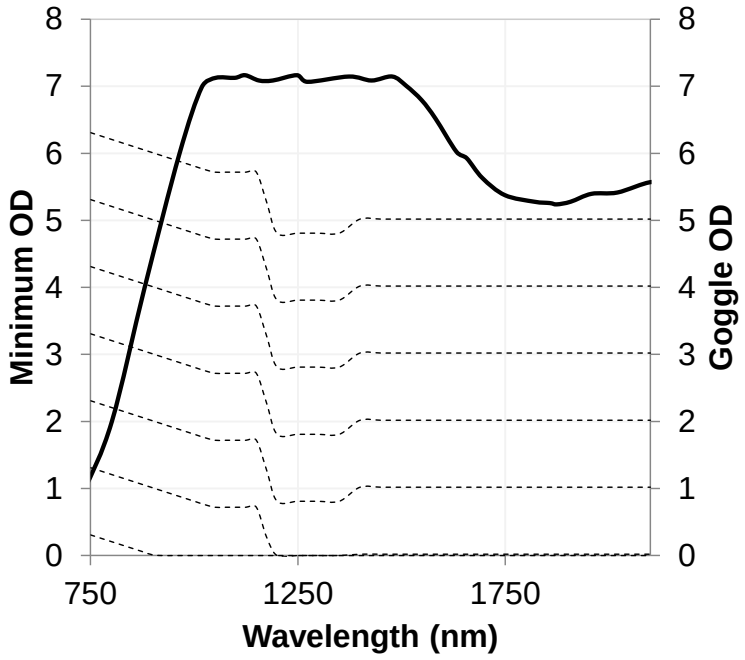

Figure 4.1: Minimum OD requirement and OD specification of Thorlabs goggles [34]

Second, the high-power laser may damage the equipment on its light path. Thus, beam stops such as a thermal pile and a block board are put in place to stop light and therefore confine the hazard to a limited area. The beam stops prevent the beam from continuing its path, making the area beyond the stops safer. Also, they stop the beam from hitting other surfaces and creating accidental or unexpected reflections.

Finally, high-power laser light cannot be directly connected or input to fiber and other power-sensitive equipment such as Optical Spectrum Analyzer (OSA) because they cannot stand such a high power input. The correct way is collecting the scattered laser light with a fiber and then it can be used in further analysis. Figure 4.2 shows this procedure with a C-mount diode laser.

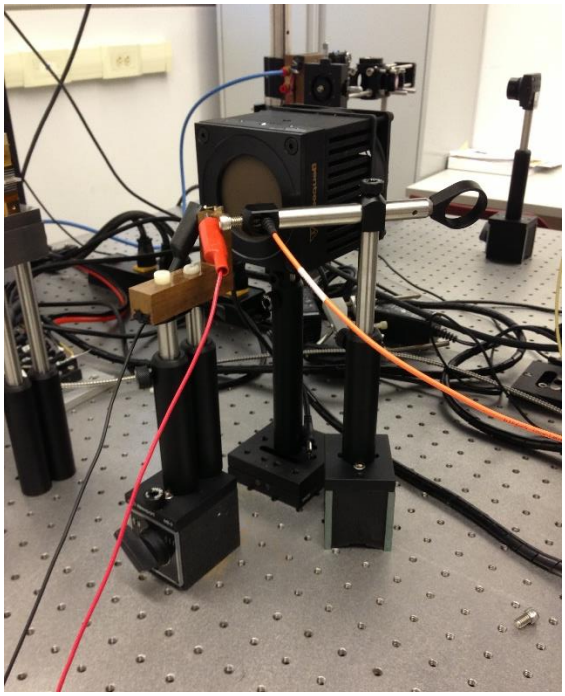

Figure 4.2: Collecting scattered high-power laser light with a fiber

Also, optical elements must be aligned and fine-tuned at very low powers before turning the lasers up to any significant fraction of the final operating powers. This helps to prevent damage to equipment and injury to personnel. Improperly focused optics can deposit too much energy in one area destroying detectors or causing lenses to break.

4.2 Experimental Verification by Output Power Measurement

Based on the model developed in the previous chapters, the output powers of a semiconductor laser with increasing injection current can be calculated. This gives us a way to check the calculation model by measuring the output powers of the simulated laser experimentally. An 808 nm high-power semiconductor laser was provided, and Table 4.1 shows its material and device parameters.

Table 4.1: Material and device parameters for the simulated 808 nm semiconductor laser

Cavity length (μm)	1500	Internal quantum efficiency η_i	0.89
Quantum well thickness (Å)	100	Optical mode Γ	0.01
Emitter width (μm)	80	Internal loss α_i (1/cm)	2.0
HR	0.98	Refractive index	3.5
PR	0.05	g_0 (1/cm)	1000
J_{tr} (A/cm^2)	121	Threshold current I_{th} (A)	0.4846
N_{tr} (1/cm^3)	1.1×10^{18}	Thermal resistance R_{th} (K/W)	8.4
T_0 (K)	110	T_1 (K)	450
σ (Ωcm^2)	2.9×10^{-5}	V_s (V)	75×10^{-3}
Spontaneous coefficient B (cm^6/s)	1×10^{-9}	Auger coefficient C (cm^9/s)	1×10^{-30}

Some of the parameters shown above, including reflectivities, internal loss, and internal quantum efficiency, are fit by comparing the calculated output power incorporated LSHB and thermal effects with the measured output power. All the parameters are within published ranges [5]. The comparison of calculated and measured output powers is shown in Figure 4.3 with injection current from 0A to 5A. These results do not prove the presence (or absence) of LSHB, but do indicate the model is reasonable.

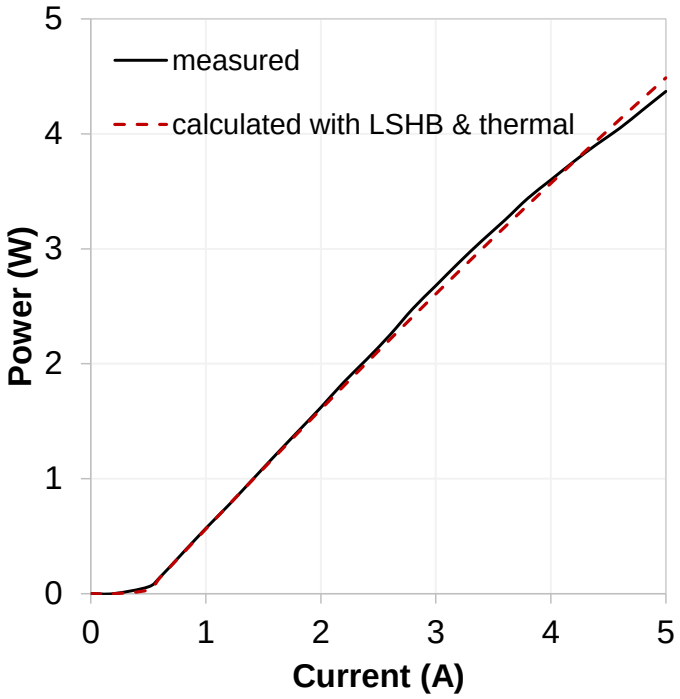

Figure 4.3: Comparison of measured and calculated output powers

4.3 Experimental Verification by Spontaneous Emission Observation

Spontaneous emission rate R_{sp} is proportional to the square of carrier density [35].

$$R_{sp} = BN^2(z) \tag{4.1}$$

This simple relationship gives us a way to observe the LSHB effect and check our calculation model. The spontaneous emission was observed from a window patterned in the top contact of the 808 nm semiconductor laser by a setup consisting of a microscope system and a CCD camera. Figure 4.4 shows the schematic experimental configuration, and the experimental setup is shown in Figure 4.5.

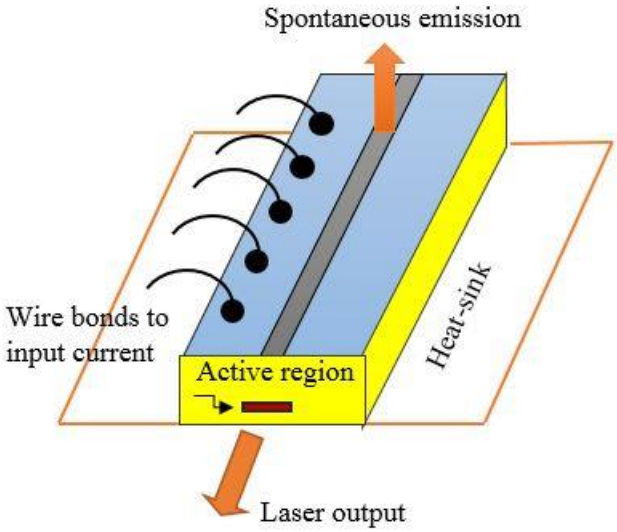

Figure 4.4: Experimental configuration of spontaneous emission observation

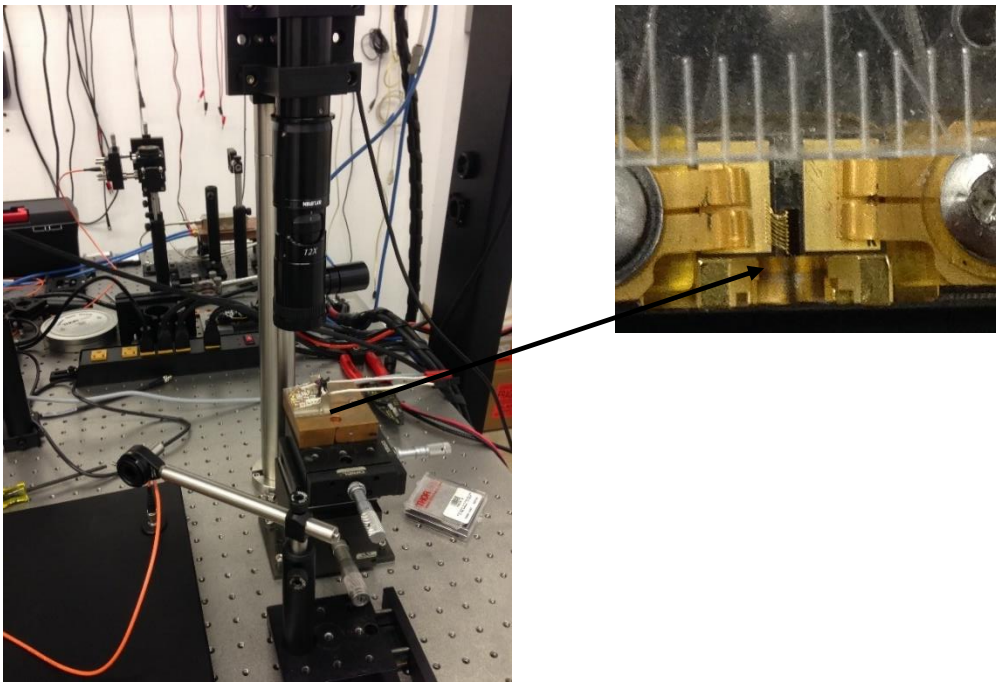

Figure 4.5: Experiment setup of the observation of spontaneous emission

The observation results are shown in Figure 4.6. Due to the scattered light near the two facets, the measurement region was focused on the middle of the laser chip.

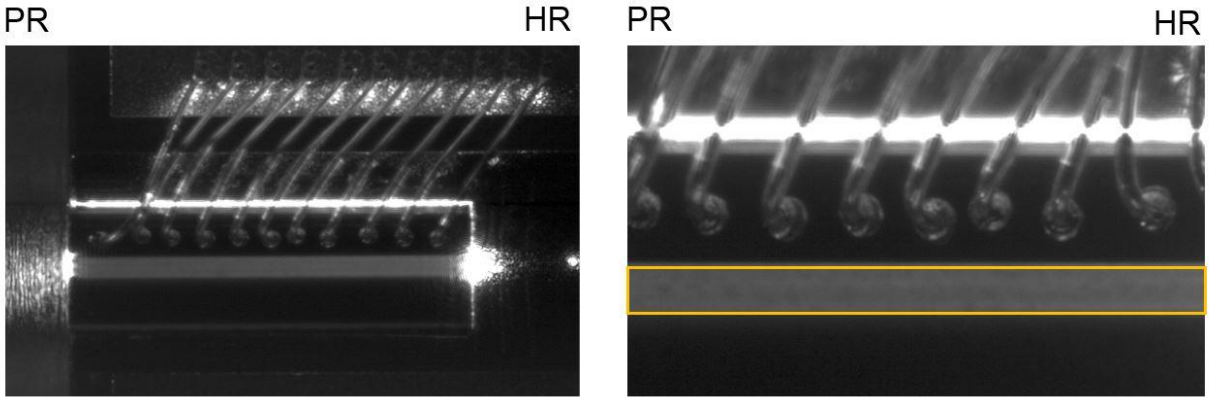

(a) (b)

Figure 4.6: Observation of spontaneous emission from the top window of an 808 nm semiconductor Laser. (a) whole chip (b) focus on central region

The average grey value for the central region was measured with increasing applied current in order to determine if scattered stimulated emission negatively affects the experimental results. As observed in Figure 4.7, below threshold current ($I_{th} = 0.48$), the spontaneous emission rate increases as injection current goes up. Once the current is beyond threshold, the average grey value reaches a nearly flat stage, which indicates carrier density, and hence gain, clamping. Notice that the measured average grey value isn't clamping perfect as a constant number corresponding the constant average threshold carrier density. This maybe a resultant of some scattered stimulated light coming out from the top window when the laser is working above threshold current. Also, self-heating causes the increase of threshold current, introduced in Chapter 3, and hence the increase of threshold carrier density, may also lead to this imperfect clamping. Nevertheless, it is

clear that the majority of light defected from this window is spontaneous emission, and as such, serves as a good indicator of the gain in the cavity.

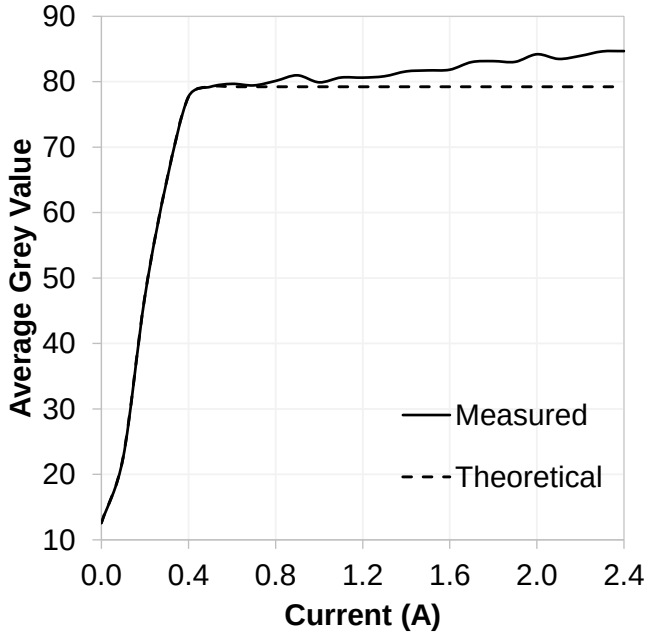

Figure 4.7: Average grey value for the central region with increasing current

The profiles of longitudinal relative grey value of the spontaneous emission for injection currents 0.7A, 1.3A, and 2.4A were compared with calculated profiles of the square of carrier density, as shown in Figure 4.8. The measured data was fit with calculated date by adjusting the axis scale to best fit one another. The square of threshold carrier density without LSHB is also shown for comparison.

As observed in Figure 4.8, the measured grey value profiles present the characteristic of non-uniformity. The spontaneous emission rate is smaller near PR facet and higher near HR facet, which experimentally demonstrates the existence of the LSHB effect in the device. For higher injection current, this non-uniformity becomes more obvious, and the measured data is more

consistent with calculated data, which demonstrates the impact of LSHB is greater at high applied currents for high-power diode lasers. Also, the measured data shows that most of light intensity we observed from the top window is spontaneous emission. If the dominant light is scattered laser light, the measured grey value at PR facet would be higher than at HR facet because the photon density is higher at PR facet. This further confirms that the dominant source of light from the top window is spontaneous emission. More importantly, the experimental results are in good fit with the calculated results, which verifies the validity of the calculation model.

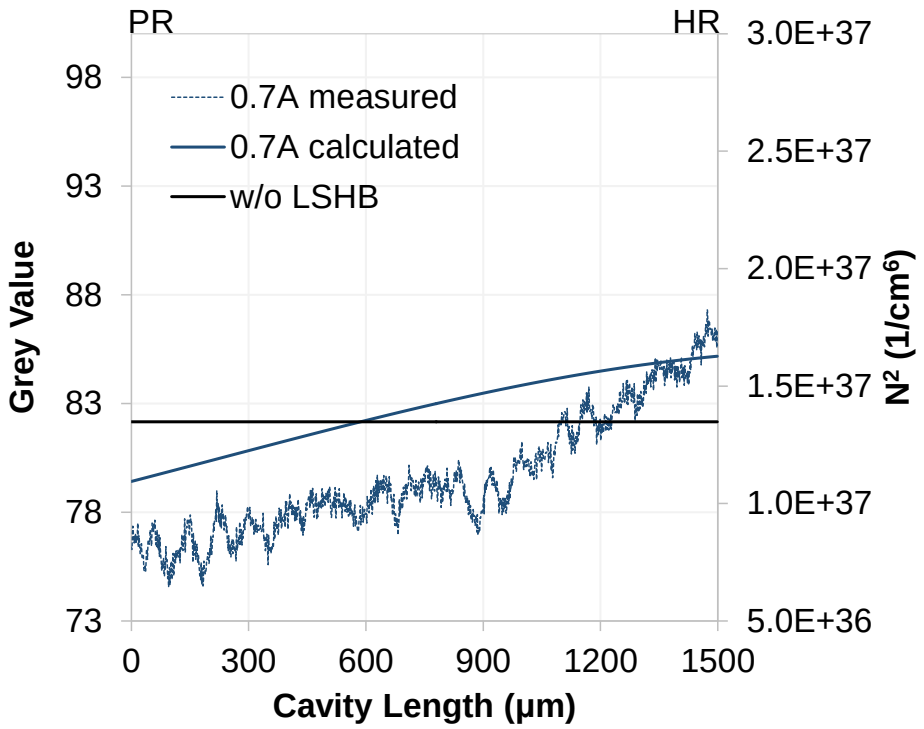

Figure 4.8: (a) Comparison of calculated and experimental results for I = 0.7A

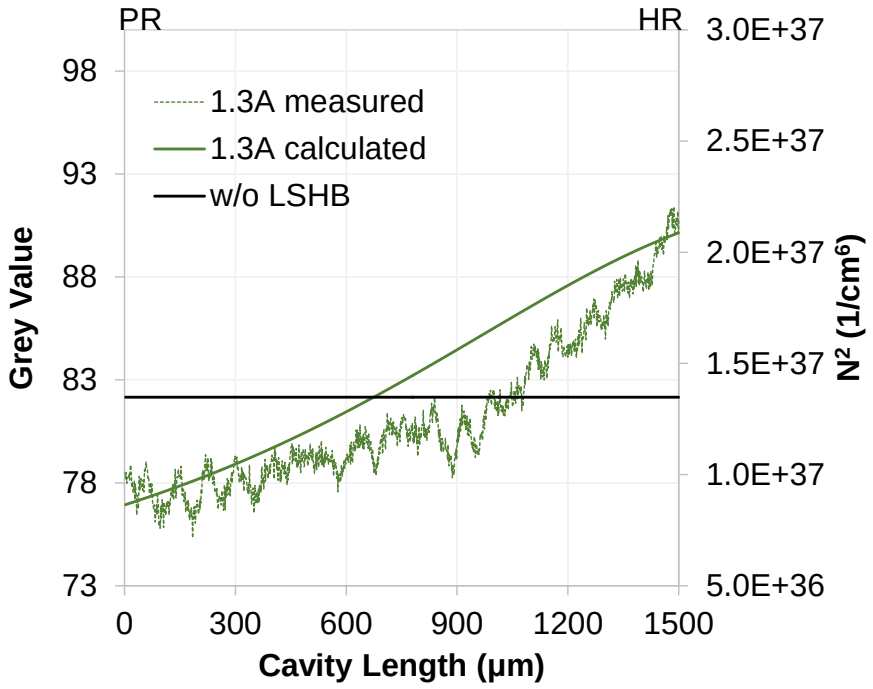

Figure 4.8: (b) Comparison of calculated and experimental results for I = 1.3A

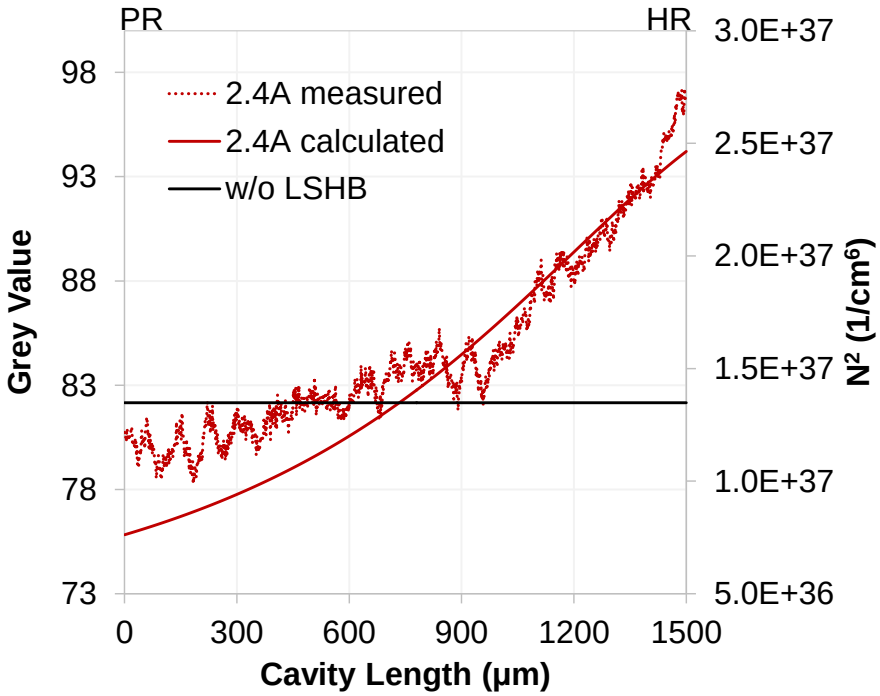

Figure 4.8: (c) Comparison of calculated and experimental results for I = 2.4A

5. CONCLUSION

5.1 Summary of Results Obtained

In conclusion, a self-consistent calculation model was built based on modified rate equations to simulate the LSHB effect in high-power semiconductor lasers. Inhomogeneous profiles of photon density, carrier density, and gain distribution have been obtained with LSHB. A calculation model without LSHB was also built for comparison. Based on the comparison, I have analyzed the magnitude of the impact of LSHB on laser output for different parameters including injection current, cavity length, and wavelength. The output powers of an example 808 nm semiconductor laser were measured and compared with calculated output powers considering LSHB and thermal effects. The results were consistent with each other. Another experimental verification was carried out by the observation of spontaneous emission. The experimental results were in agreement with calculation results. Thus, the validity of the calculation model and the existence of LSHB in high-power semiconductor lasers have been experimentally demonstrated.

This work is useful in providing an effective calculation model incorporated LSHB and thermal effect which can be used to calculate and analyze the physical processes in the high-power semiconductor lasers. The analysis part of this work presents an intuitionistic description of the magnitude of the impact of LSHB with the change of other parameters, which contributes to the further design and fabrication of high-power semiconductor lasers. The experimental work provides an effective method to observe and verity LSHB experimentally, which can also be used in other works related to LSHB.

5.2 Future Work

In this thesis, LSHB is calculated and shown to limit the output power of high-power semiconductor lasers. Future work should focus on the mitigation of LSHB, in order to enable power improvement. One possible approach is by design waveguide confinement to mitigate the inhomogeneous photon density in the cavity. Based on the calculation result mentioned before, the photon density is higher near PR facet while it is lower near HR facet. By designing a waveguide structure that expands near PR facet and shrinks near HR facet, the photon density can be modified to be more homogeneous. One possible waveguide structure is shown in Figure 5.1.

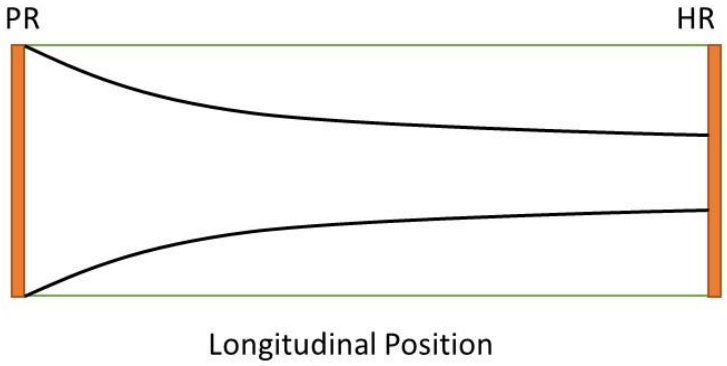

Figure 5.1: One of the waveguide structure that contributes to mitigate LSHB

The calculation model developed in this thesis can also be used in this new calculation by adding a spatially varying width parameter. Experimental work can also be carried out using the same method presented in this thesis to observe if the inhomogeneous carrier density is reduced.

LIST OF REFERENCES

[1] David F. Welch. "A brief history of high-power semiconductor lasers." IEEE Journal of Selected Topics in Quantum Electronics, Vol. 6, No. 6, (2000). Print.

[2] Katz, J. "Power conversion efficiency of semiconductor injection lasers and laser arrays in CW operation." IEEE Journal of Quantum Electronics, Vol. 21, Issue. 12, 1854-1857, (2003). Print.

[3] Sony Company, "Tohoku University and Sony Corporation jointly develop the world's first blue-violet ultrafast pulsed semiconductor laser with 100 watt output." July 20, 2010. Web. <http://www.sony.net/SonyInfo/News/Press/201007/10-0720E>

[4] Paul Leisher and Steve Patterson. "DEPS short course of introduction to high power semiconductor lasers for directed energy applications." June 24, 2013. Lecture notes.

[5] L. A. Coldren and S. W. Corzine. "Diode lasers and photonic integrated circuits." John Wiley & Sons, ISBN 0-471-11875-3, New York, (1995). Book.

[6] Photonics Media. "High-power semiconductor lasers." Photonics Handbook, Web. <http://www.photonics.com/EDU/Handbook.aspx?AID=25169>

[7] Farhan Rana. "Semiconductor Optoelectronics." Cornell University. Lecture notes.

[8] ECE495 Photonic Device Laboratory. "Edge-emitting semiconductor lasers." University of Illinois at Urbana-Champaign. Lecture notes.

[9] Wikipedia. "Facet-view diagram of simple separate-confinement-heterostructure quantum-well laser diode." Web. <http://en.wikipedia.org/wiki/File:Simple_sch_laser_diode.svg>

[10] Michael Bass, Eric W. Van Stryland, David R. Williams, and William L. Wolfe. "Handbook of Optics." McGRAW-HILL, INC. (1995). Book.

[11] Pablo V. Mena, Sung-Mo Kang, and Thomas A. DeTemple. "Rate-equation-based laser models with a single solution regime." Journal of lightwave technology, Vol.15, No.4, April 1997. Print.

[12] Shun Lien Chuang. "Physics of optoelectronic devices." Wiley Series in Pure and Applied Optics, ISBN 0-471-10939-8, New York, (1995). Book.

[13] Robert F. Pierret. "Semiconductor Device Fundamentals." Addison-Wesley Publishing Company, Inc. (1996). Book.

[14] B. S. Ryvkin and E. A. Avrutin. "Spatial hole burning in high-power edge-emitting lasers: a simple analytical model and the effect on laser performance." Journal of applied physics, 043101 (2011). Print.

[15] J. L. Pleumeekers, M. A. Dupertuis, T. Hessler, P. E. Selbmann, S. Haacke, and B. Deveaud. “Longitudinal spatial hole burning and associated nonlinear gain in gain-clamped semiconductor optical amplifiers.” IEEE Journal of Quantum Electronics, Vol. 34, No.5, May 1998. Print.

[16] H Wenzel, P Crump, A Pietrzak, X Wang, G Erbert and G Trankle. “Theoretical and experimental investigations of the limits to the maximum output power of laser diodes.” New Journal of Physics, 085007 (2010). Print.

[17] Wei-chiao W. Fang, C. G. Bethea, Y. K. Chen, and Shun Lien Chuang. “Longitudinal spatial inhomogeneities in high-power semiconductor lasers.” IEEE Journal of selected topics in quantum electronics, Vol. 1, No. 2, June 1995. Print.

[18] Jan Pomplun, Sven Burger, Frank Schmidt, Andrei Schliwa, Dieter Bimberg, Agnieszka Pietrzak, Hans Wenzel, and Gotz Erbert. “Finite element simulation of the optical modes of semiconductor lasers.” Physics. Optics, No. 4, 846-853 (2010). Print.

[19] Wikipedia, “Numerical methods for ordinary differential equations.” Web. <http://en.wikipedia.org/wiki/Numerical_methods_for_ordinary_differential_equations>

[20] C. G. Bethea. “Spatially imaged inhomogeneous spontaneous emission spectra of high power in InGaAsP/InP Fabry-Perot lasers.” Appl. Phys. Lett. 67 (2). 10 July 1995. Print.

[21] H. J. Wunsche, U. Bandelow, and H. Wenzel. “Calculation of combined lateral and longitudinal spatial hole burning in λ/4 shifted DFB lasers.” IEEE Journal of Quantum Electronics, Vol. 29, No. 6, June 1993. Print.

[22] “Two-and three-dimensional semiconductor analysis package” Software. <http://www.wias-berlin.de/software/tescal/>

[23] F. Rinner, J. Rogg, P. Friedmann, M. Mikulla, and G. Weimann. “Longitudinal carrier density measurement of high power broad area laser diodes.” Applied Physics Letters. Vol. 80, No. 1, 7 January 2002. Print.

[24] Zhigang Chen, Ling Bao, John Bai, Mike Grimshaw, Rob Martinsen, Mark DeVito, Jim Haden and Paul Leisher. “Performance limitation and mitigation of longitudinal spatial hole burning in high-power diode lasers.” Proc. SPIE 8277, Novel In-Plane Semiconductor Lasers XI, 82771J, February 9, 2012. Print.

[25] Wikipedia. “Newton’s method” Web. <http://en.wikipedia.org/wiki/Newton's_method>

[26] M. Rattunde, C. Mermelstein, J. Schmitz, R. Kiefer, W. Pletschen, M. Walther, and J. Wagner. “Comprehensive modeling of the electro-optical-thermal behavior of (AlGaIn)(AsSb)-based 2.0 μm diode lasers.” Applied Physics Letters, Vol. 80, No. 22, 3 June 2002. Print.

[27] Wikipedia. “Thermal resistance” Web.<http://en.wikipedia.org/wiki/Thermal_resistance>

[28] E. Marin, I. Camps, M. Sanchez and P. Diaz. “Thermal resistance of double heterostructure separate confinement GaAs/ AlGaAs semiconductor lasers in stripe geometry configuration.” Revista Mexicana de Fisica 42, No. 3 (1996). Print.

[29] Henning Riechert, Arun Ramakrishnan and Gunther Steinle. “Development of InGaAsN-based 1.3 μm VCSELs.” Semiconductor Science and Technology, Vol. 17, No.8, 17 July 2002. Print.

[30] Hongping Zhao, Guangyu Liu, Jing Zhang, Ronald A. Arif, and Nelson Tansu. “Analysis of internal quantum efficiency and current injection efficiency in III-Nitride light-emitting diodes.” Journal of Display Technology, Vol.9, No.4, April 2013. Print.

[31] Bernd Kohler, Heiko Kissel, Marco Flament, Paul Wolf, Thomas Brand, Jens Biesenbach. “High-power diode laser modules from 410 nm- 2200 nm.” Proc. of SPIE Vol. 7583 75830F-1. Print.

[32] Fred Seeber. “Fundamentals of Photonics, Module 1.2, Light sources and laser safety.” SPIE document. Ebook.

[33] Laser Institute of America. “OD calculation tool” Web. <https://www.lia.org/evaluator/od.php>

[34] Colin EW Rice. “Lab Safety OD Requirements” Rose-Hulman Institute of Technology.

[35] Ali Guermache, Vincent Voiriot, Damien Locatelli, Frederic Legrand, Rose-Marie Capella, Philippe Gallion, and Joel Jacquet. “Experimental demonstration of spatial hole burning reduction leading to 1480 nm pump lasers output power improvement.” IEEE Photonics Technology Letters, Vol. 17, No. 10, October 2005. Print.

Appendix A: Rate Equation Calculation with Classic Solutions

```
> restart :
>
> # Define parameters
> h := 6.62·10^-34 : λ := 980·10^-9 : c := 3·10^8 :
> q := 1.6·10^-19 : g0 := 1800 : Ntr := 2.2·10^18 :
> ai := 1 : am := 3.837 : Γ1 := 0.01 :
> ni := 0.95 : V := 1.8·10^-9 : τe := 10^-9 :
> vg := 8.57·10^9 : τp := 2.412·10^-11 :
> # Solve threshold carrier density
> g := g0·ln(N/Ntr) :
> equation1 := 0 = Γ1·vg·g·Np - Np/τp :
> Nth := solve(equation1, N);
                        Nth := 2.878358862 10^18
> # Solve threshold gain
> gth := evalf(subs(N = Nth, g));
                        gth := 483.7732769
> # Solve threshold current
> Ith := Nth·q·V/(τe·ni);
                        Ith := 0.8725972128
> # Solve photon density
> equation2 := 0 = ni·I1/(q·V) - Nth/τe - vg·gth·Np :
> Np := solve(equation2, Np);
                Np := 7.956249997 10^14 I1 - 6.942601573 10^14
> # Solve output power - Method 1
> Poutput := Np·V·100· h·c·vg·am/λ;
                Poutput := 0.9543478852 I1 - 0.8327613048
> plot(Poutput, I1 = Ith ..10);
```

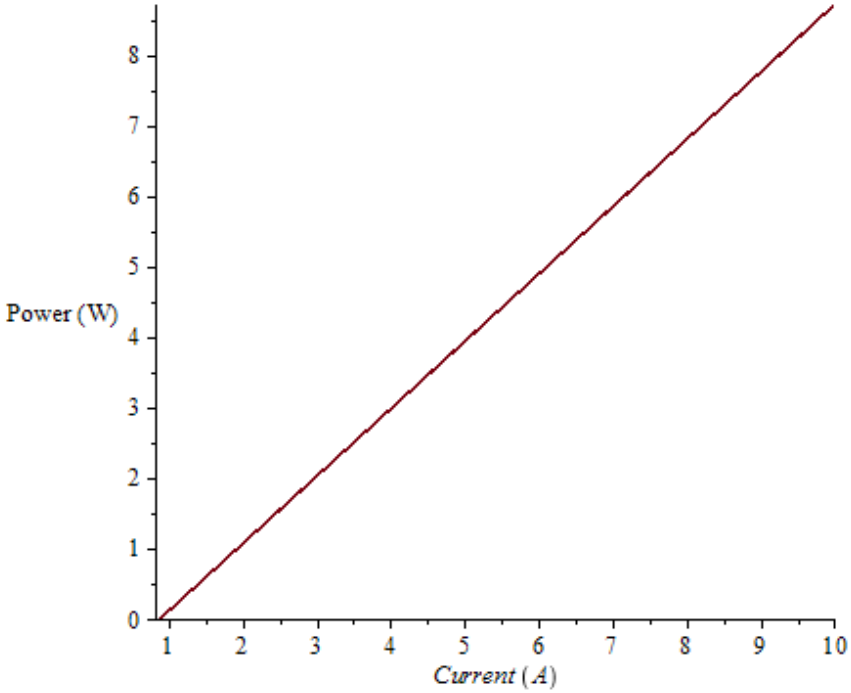

> **# Solve output power - Method 2**

> $Poutput2 := \frac{h \cdot c \cdot ni}{\text{lambda} \cdot q} \cdot \frac{am}{am + ai} \cdot (I1 - Ith);$

$$Poutput2 := 0.9544924619\ I1 - 0.8328874619$$

> $plot(Poutput2, I1 = Ith..10);$

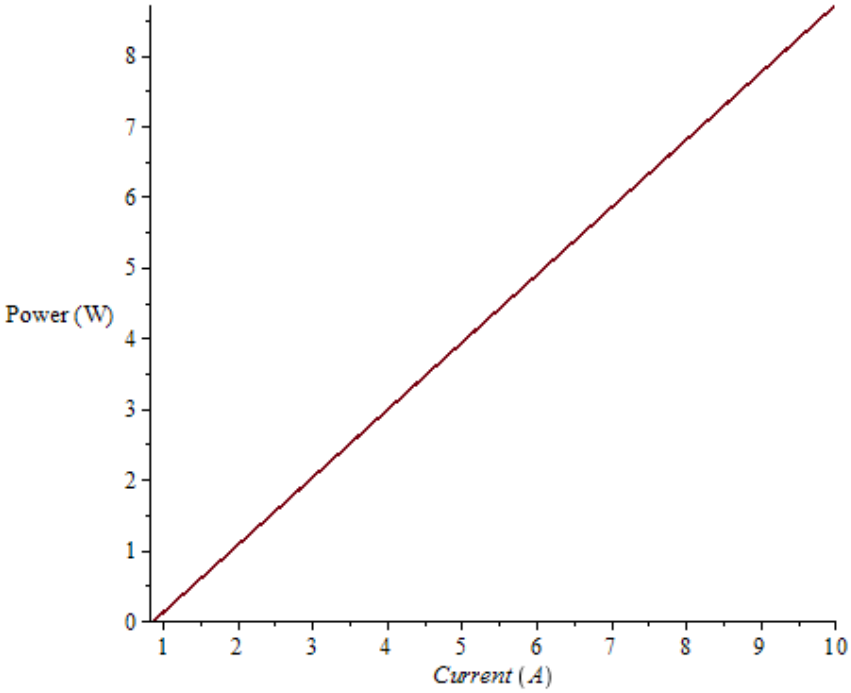

Appendix B: Finite Difference Method Solving One-Dimensional Heat Equation

```
%Finite Difference method solving 1D steady state heat equation

l=1;                            %the lengh of the copper stick is 1m
detx=0.01;                      %the lengh of each segment is 0.01m
n=1+l/detx;
q1=25;                          %the temperature at one end is 25
qcenter=-100000*(detx)^2/401; %heat source is 1W at the middle point
qn=25;                          %the temperature at another end is 25

%solve finite difference heat equation by matrix
M=zeros(n,n);
Q=zeros(n,1);

%populate Q
Q(1)=q1;
Q((n+1)/2)=qcenter;
Q(n)=qn;

%populate M
M(1,1)=1;
M(n,n)=1;
for i=2:n-1
    M(i,i+1)=1;
    M(i,i)=-2;
    M(i,i-1)=1;
End

T=inv(M)*Q;
plot(T);
xlabel('Longitudinal Position');
ylabel('Temperature');
```

Appendix C: Matlab Code for 1475 nm Semiconductor Laser Calculation

Main Program:

```
clc;
close all;
clear all;

%Define global constants
q=1.6*10^-19;  %electron charge [C]
c=3*10^8;      %speed of light [m/s]
h=6.626*10^-34;%Plank's constant [J*s]

%Define device constants
d=140;         %quantem well thickness [A.]
L=3800;        %cavity length [um]
W=150;         %emitter width [um]
R1=0.005;      %PR reflection (at z=0)
R2=0.99;       %HR reflection (at z=L)
ni=0.87;       %internal quantum efficiency
Gamma=0.01;    %optical mode parameter
ai=2;          %internal loss [1/cm]
index=3.5;     %effective index of optical mode
g0=1000;       %g=g0*ln(N/Ntr) [1/cm]
Jtr=121;       %transparency current density [A/cm^2]
Ntr=1.*10^18; %transparency carrier density [1/cm^3]
lambda=1475;   %wavelength [nm]
Rth=2.2;       %thermal resistance [K/W]
T0=50;         %temperature parameter
T1=150;        %temperature parameter

% voltage = 1240/lambda + J*Sigma + Vs*Ln(J/Jdiode) + Rs*I
Sigma = 7.8*10^-5; %in Ohm*cm^2
Vs = 22*10^-3;     %in V
J_diode = 80;      %in A/cm^2

%Define parameters which can be calculated
vg=c/index*100;                   %group velocity [cm/s]
am=1/(2*L*10^-4)*log(1/(R1*R2)); %loss at the mirrors [1/cm]
gth=(ai+am)/Gamma;                %threshold gain [1/cm]
Nth=Ntr*exp(gth/g0);              %threshold carrier density [1/cm^3]
taop=1/((ai+am)*vg);              %photon lifetime [s]
V=d*L*W*10^-16;                   %volume [cm^3]
A=Jtr*ni/(q*d*10^-8*Ntr);         %Shockley-Read_Hall coefficient [1/s]
B=0;                              %spontaneous recombinition coefficient
C=0;                              %Auger coefficient
Ith=(A*Nth+B*Nth^2+C*Nth^3)*q*d*L*W*(10^-16)/ni;%threshold current
I_diode=J_diode*L*W*10^-8;

%Define simulation constants
grid=200;      %number of grid in z direction
```

```
dz=L/grid;      %grid resolution in z direction [um]
I=[2,5,10];     %Injection current [A]
F=10^-8;        %control parameter used in Newton's method
for i=1:length(I)
N=zeros(i,1+grid);  %carrier density
G=zeros(i,1+grid);  %gain
NptotalLSHB=zeros(i,1+grid); %photon density with LSHB
NppositiveLSHB=zeros(i,1+grid);
NpnegativeLSHB=zeros(i,1+grid);
Nptotal=zeros(i,1+grid);     %photon density without LSHB
Npforward=zeros(i,1+grid);
Npbackward=zeros(i,1+grid);
end

%with LSHB
for i=1:length(I)

   if I(i)<=Ith;
     for j=1:1+grid
         NptotalLSHB(i,j)=0;
         syms Nx
         eqN = ni*I(i)/(q*V) - A*Nx - B*Nx^2 - C*Nx^3-
vg*g0*log(Nx/Ntr)*NptotalLSHB(i,j);
         N(i,j)=solve(eqN==0,Nx);
         G(i,j)=g0*log(N(i,j)/Ntr);
     end
   end

   if I(i)>Ith;
       %guess Npositive at facet R1
       NppositiveGuess=((ni*(I(i)-Ith)/q/V)/(vg*gth))*R1/(1+R1);
       %solve Np,N,G along z under first guess
       [errorLSHB,~,~,~,~]=solveLSHB(NppositiveGuess,I(i));

       %Newton's method to reduce error
       Count=1;j=1;
       Guess=zeros(1,1+grid);Guess(1)=NppositiveGuess;
         while errorLSHB>10^-8;
          [errorLSHB2]=solveLSHB(Guess(j)+F*Guess(j),I(i));
          Guess(j+1)=Guess(j)-errorLSHB*F*Guess(j)/(errorLSHB2-errorLSHB);

[errorLSHB,NppositiveLSHB_temp,NpnegativeLSHB_temp,N_temp,G_temp]=solveLSHB(G
uess(j+1),I(i));
          j=j+1;
          Count=Count+1;
            if Count>20
               break
            end
         end
      NppositiveLSHB(i,1:1+grid)=NppositiveLSHB_temp;
      NpnegativeLSHB(i,1:1+grid)=NpnegativeLSHB_temp;

NptotalLSHB(i,1:grid+1)=NppositiveLSHB(i,1:1+grid)+NpnegativeLSHB(i,1:1+grid)
;
```

```
      N(i,1:grid+1)=N_temp;
      G(i,1:grid+1)=G_temp;
   end

end
H=0.01;
% without LSHB
for i=1:length(I)
    if I(i)>Ith;
      %Guess Np+ at facet R1
      Nppositive=NptotalLSHB(i,1)*R1/(1+R1);
      Npaverage=(ni*(I(i)-Ith)/q/V)/(vg*gth);
      %solve Np+ and Np- for constant gain
      [error,Total]=solveNp(Nppositive,Npaverage);
      %Newton's method to reduce error
      Count=1;j=1;Guess=zeros(1,1+grid);Guess(1)=Nppositive;
      while error>10^-8
          [error2]=solveNp(Guess(j)+H*Guess(j),Npaverage);
          Guess(j+i)=Guess(j)-error*H*Guess(j)/(error2-error);
          [error,Total,Forward,Backward]=solveNp(Guess(j+1),Npaverage);
          j=j+1;
          Count=Count+1;
              if Count>20
                  break
              end
      end
      Npforward(i,1:1+grid)=Forward;
      Npbackward(i,1:1+grid)=Backward;
      Nptotal(i,1:1+grid)=Total;
    end
end

%thermal effect initiate variable
i=length(I);
V=zeros(i);  %voltage
Pin=zeros(i);%input power
Pout_LSHB=zeros(i); %output power
Pout=zeros(i);      %output power w/o LSHB
PoutLSHB_thermal=zeros(i);
Pout_thermal=zeros(i);
Ithreshold=zeros(i); %threshold current
IthLSHB_thermal=zeros(i);
Ithr=zeros(i);
Ith_thermal=zeros(i);
nd_LSHB=zeros(i); %DQE
nd=zeros(i);
ndLSHB_thermal=zeros(i);
nd_thermal=zeros(i);
WPE=zeros(i); %power efficiency
WPE_LSHB=zeros(i);
WPELSHB_thermal=zeros(i);
WPE_thermal=zeros(i);

for i=1:length(I)
```

```
  %calculate voltage
  if I(i)<I_diode
      V(i)=h*c/(lambda*10^-9)/q+I(i)/(L*W*10^-8)*Sigma;
  else
      V(i)=h*c/(lambda*10^-9)/q+I(i)/(L*W*10^-8)*Sigma+Vs*log(I(i)/I_diode);
  end

  Pin(i)=V(i)*I(i); %calculate input power
  %calculate LSHB output power
  Pout_LSHB(i)=NpnegativeLSHB(i,1)*(d*10^-8)*(W*10^-4)*h*c/(lambda*10^-
9)*vg*(1-R1)/Gamma + NppositiveLSHB(i,end)*(d*10^-8)*(W*10^-
4)*h*c/(lambda*10^-9)*vg*(1-R2)/Gamma;
  %calculate output power w/o LSHB
  Pout(i)=Npbackward(i,1)*(d*10^-8)*(W*10^-4)*h*c/(lambda*10^-9)*vg*(1-
R1)/Gamma + Npforward(i,end)*(d*10^-8)*(W*10^-4)*h*c/(lambda*10^-9)*vg*(1-
R2)/Gamma;

  WPE_LSHB(i)=Pout_LSHB(i)/Pin(i);%LSHB power efficiency
  WPE(i)=Pout(i)/Pin(i);%power efficiency w/o LSHB

  %calculate Ithreshold with LSHB
  Ithsum=0;
  for j=1:1+grid
    Ithsum=Ithsum+(A*N(i,j)+B*N(i,j)^2+C*N(i,j)^3)*q*d*L*W*10^-16/ni;
  end
  Ithaverage=Ithsum/grid;
  Ithreshold(i)=Ithaverage;
  Ithr(i)=Ith;
  %calculate DQE
  nd_LSHB(i)=Pout_LSHB(i)/(h*c/(lambda*10^-9)/q*(I(i)-Ithreshold(i)));
  nd(i)=Pout(i)/(h*c/(lambda*10^-9)/q*(I(i)-Ith));

  deltaT1=Rth*(Pin(i)-Pout_LSHB(i));
  deltaT2=Rth*(Pin(i)-Pout(i));
  IthLSHB_thermal(i)=Ithreshold(i)*exp(deltaT1/T0);
  Ith_thermal(i)=Ith*exp(deltaT2/T0);
  ndLSHB_thermal(i)=nd_LSHB(i)*exp(-deltaT1/T1);
  nd_thermal(i)=nd(i)*exp(-deltaT2/T1);
  PoutLSHB_thermal(i)=ndLSHB_thermal(i)*(h*c/(lambda*10^-9)/q*(I(i)-
IthLSHB_thermal(i)));
  Pout_thermal(i)=nd_thermal(i)*(h*c/(lambda*10^-9)/q*(I(i)-Ith_thermal(i)));

  WPELSHB_thermal(i)=PoutLSHB_thermal(i)/Pin(i);
  WPE_thermal(i)=Pout_thermal(i)/Pin(i);

End
```

Function Program 1:

```
%Finite Difference Method of solving Np(z)with LSHB
function
[error,NppositiveLSHB,NpnegativeLSHB,N,G]=solveLSHB(Nppositive_at_R1,I)
%Define global constants
q=1.6*10^-19;  %electron charge [C]
c=3*10^8;      %speed of light [m/s]

%define parameters
d=140;         %quantem well thickness [A.]
L=3800;        %cavity length [um]
W=150;         %emitter width [um]
R1=0.005;      %PR reflection (at z=0)
R2=0.99;       %HR reflection (at z=L)
ni=0.87;       %internal quantum efficiency
Gamma=0.01;    %optical mode parameter
ai=2;          %internal loss [1/cm]
index=3.5;     %effective index of optical mode
g0=1000;       %g=g0*ln(N/Ntr) [1/cm]
Ntr=1.1*10^18;%transparency carrier density [1/cm^3]
Jtr=121;       %transparency current density [A/cm^2]

%Define parameters which can be calculated
vg=c/index*100;                  %group velocity [cm/s]
V=d*L*W*10^-16;                  %volume [cm^3]
A=Jtr*ni/(q*d*10^-8*Ntr);        %Shockley-Read_Hall coefficient [1/s]
B=0;                             %spontaneous recombinition coefficient
C=0;

%Define simulation constants
grid=200;      %number of grid in z direction
dz=L/grid;     %grid resolution in z direction [um]

%setup vectors
n=1+grid;
NppositiveLSHB=zeros(1,n);
NpnegativeLSHB=zeros(1,n);
NptotalLSHB=zeros(1,n);
N=zeros(1,n);
G=zeros(1,n);

%Np positive at the facet R1
NppositiveLSHB(1)=Nppositive_at_R1;
%Np negative at the facet R1
NpnegativeLSHB(1)=NppositiveLSHB(1)/R1;
%Np total at the facet R1
NptotalLSHB(1)=NppositiveLSHB(1)+NpnegativeLSHB(1);

%solve for carrier density at the facet R1
syms Nx
eqN = ni*I/V/q-A*Nx-B*Nx^2-C*Nx^3-vg*g0*log(Nx/Ntr)*NptotalLSHB(1);
```

```
N(1)=solve(eqN,Nx);

%solve for gain at the facet R1
G(1)=g0*log(N(1)/Ntr);

%solve Np,N,G along z
     for j=2:n
        NppositiveLSHB(j)=NppositiveLSHB(j-1)*(1+(dz*10^-4)*(Gamma*G(j-1)-
ai));
        NpnegativeLSHB(j)=NpnegativeLSHB(j-1)*(1-(dz*10^-4)*(Gamma*G(j-1)-
ai));
        NptotalLSHB(j)=NppositiveLSHB(j)+NpnegativeLSHB(j);

        eqN = @(Nx)ni*I/V/q-A*Nx-B*Nx^2-C*Nx^3-
vg*g0*log(Nx/Ntr)*NptotalLSHB(j);
        N(j)=fzero(eqN,N(j-1));
        G(j)=g0*log(N(j)/Ntr);

     end
     ResidualLSHB=abs(NppositiveLSHB(n)*R2-NpnegativeLSHB(n));
     error=ResidualLSHB/NpnegativeLSHB(n);
end
```

Function Program 2:

```
function [error,Total,Npforward,Npbackward]=solveNp(Nppositive,Npaverage)

L=3800;
grid=200;
dz=L/grid;
R1=0.005;
R2=0.99;
Gamma=0.01;
ai=2;
am=1/(2*L*10^-4)*log(1/(R1*R2));
gth=(ai+am)/Gamma;

n=1+grid;
Npforward=zeros(1,n);
Npbackward=zeros(1,n);
%Np positive at the facet R1
Npforward(1)=Nppositive;
%Np negative at the facet R1
Npbackward(1)=Npforward(1)/R1;
for j=2:n
        Npforward(j)=Npforward(j-1)*(1+(dz*10^-4)*(Gamma*gth-ai));
        Npbackward(j)=Npbackward(j-1)*(1-(dz*10^-4)*(Gamma*gth-ai));
end
Total=Npforward+Npbackward;
```

```
%Calculate the residual error
Npsum=0;
for j=1:n
    Npsum=Npsum+Total(j);
end
Residual=abs(Npsum/grid-Npaverage);
error=Residual/Npaverage;
end
```